Origin of the Qiyugou gold deposit in the southern margin of the North China Craton: Insights from trace elements of pyrite and mineralogy of Bi-minerals

Qiang Wu [a,b,c], Tai-Ping Zhao [a,c,*], Wei Terry Chen [d], Xin-Yu Gao [e], Lei Meng [a,c], Wenhong Johnson Qiu [f]

[a] Key Laboratory of Mineralogy and Metallogeny, Guangzhou Institute of Geochemistry, Chinese Academy of Sciences, Guangzhou 510640, China
[b] University of Chinese Academy of Sciences, Beijing 100039, China
[c] CAS Center for Excellence in Deep Earth Science, Guangzhou 510640, China
[d] State Key Laboratory of Ore Deposit Geochemistry, Institute of Geochemistry, Chinese Academy of Sciences, Guiyang 550081, China
[e] Guangdong Polytechnic of Water Resources and Electric Engineering, Guangzhou 510635, China
[f] Institute of Science and Environment (ISE), University of Saint Joseph, Macao SAR 999078, China

ARTICLE INFO

ABSTRACT

The Qiyugou gold deposit, located in the Xiong' ershan area of the North China Craton, contains abundant bismuth-sulfosalts that are closely associated with gold mineralization. Pyrite is the dominant Au-hosted mineral, and has been formed in three generations (Py1, Py2, and Py3). Py1 grains, generally intergrown with milky quartz, are coarse (>1 mm), euhedral in shape, and Au-depleted in composition. In contrast, subhedral Py2 grains, associated with light gray quartz, are medium to coarse (0.2–3 mm) and are enriched in gold that is both invisible and visible. Py3 grains (0.1–0.5 mm), intergrown with abundant sulfide minerals, are relatively fine and Au-depleted. The time-resolved LA-ICP-MS depth profiles of the Py2 grains indicate that invisible gold occurs as either solid solution or nano-particles of native gold and electrum. Visible gold occurs as small blebs in the Py2 grains where inclusions of native bismuth, galenobismutite, lillianite homologs, tetradymite, and galena are also present. In addition, it is common that electrum in microfracture infillings or along grain boundaries of the Py1 and Py2, are intergrown with bismuthinite derivatives, Bi-Cu sulfosalts, emplectite, tetradymite, chalcopyrite, galena, and Py3.

Based on textural relationships and mineral assemblages, calculation of physicochemical conditions show that gold was formed in conditions of $fTe_2 = \sim10^{-11}$ and $fS_2 = \sim10^{-11}$ to 10^{-12} for Py2, and $fTe_2 = \sim10^{-9}$ to 10^{-11} and $fS_2 = \sim10^{-10}$ to 10^{-11} for Py3. We thus proposed that such physicochemical conditions may have triggered the precipitation of Bi melt, and sulfidation driven by cooling or increase in sulfur content results in the transformation of the Au-Bi liquid into a stable assemblage of native gold and bismuthinite. These bismuth minerals are associated with native gold/Au-bearing minerals, indicating that the Au mineralization of the Qiyugou gold deposit might be genetically associated with Bi melt. The present study highlights the role of Bi as important gold scavengers in arsenic-deficient ore-forming fluid.

1. Introduction

Gold deposits containing low As but anomalously high concentrations of bismuth have attracted considerable attentions in scientific communities (Buzatu et al., 2015; Chapman et al., 2017; Ciobanu et al., 2010; Cook et al., 2009a; Oberthür and Weiser, 2008; Törmänen and Koski, 2005; Zhou et al., 2018). Based on available studies, such a common association of Au and Bi could be explained by the hypothesis that Bi melt is an effective Au collector (Douglas et al., 2000; Tooth et al., 2011). Furthermore, as bismuth-sulfosalts and tellurides assemblages are sensitive to physical–chemical fluctuations, diversity of Bi-minerals that are closely associated with Au can also provide important physicochemical information on Au ore-formation (Ciobanu et al., 2010; Cook et al., 2009b; Liu et al., 2013; Meng et al., 2020; Xu et al., 2014).
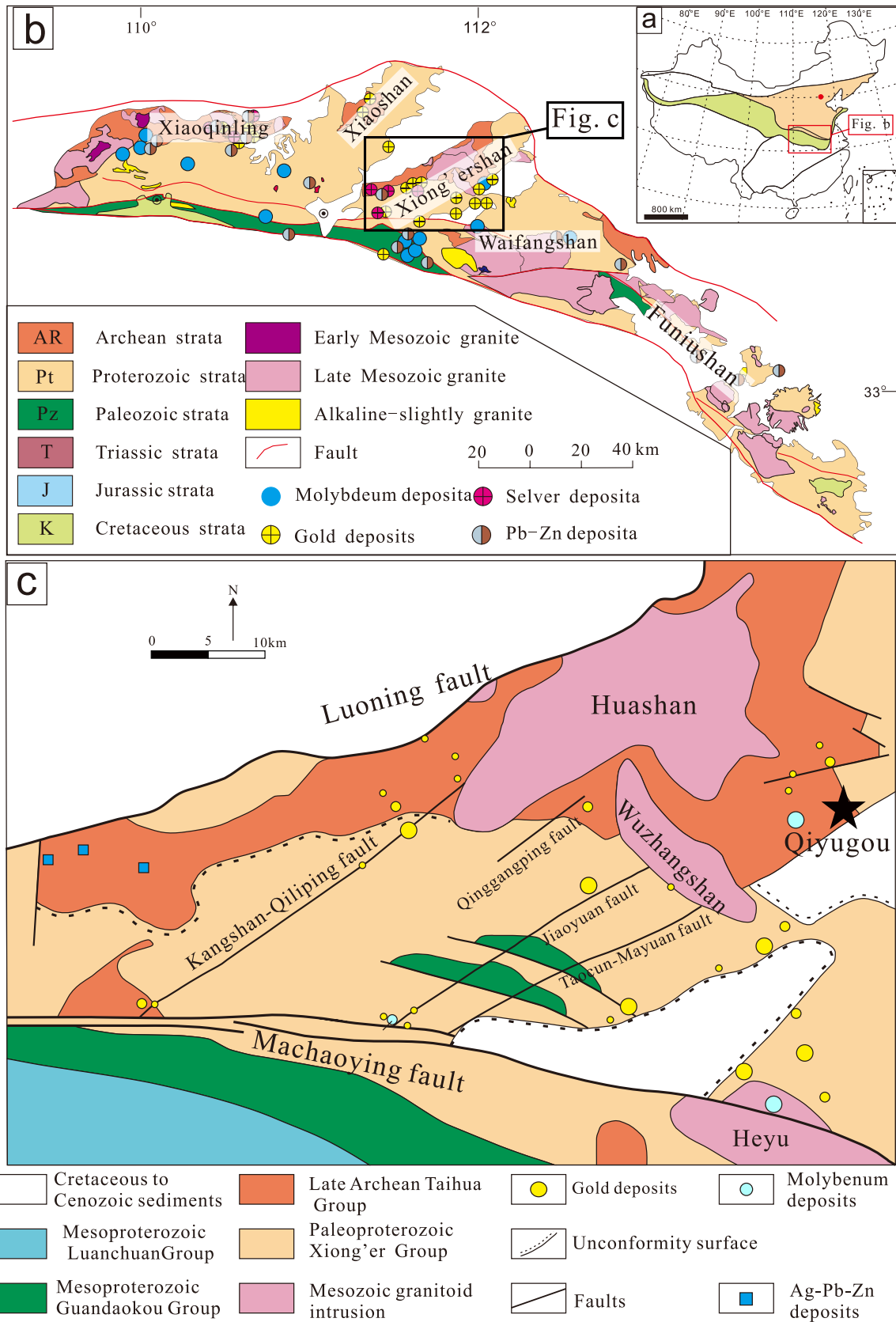
Fig. 1. (a) Major Tectonic outlines of China and (b) tectonic setting of the southern margin of the North China Craton, modified after Zhao et al. (2018); (c) geological and tectonic map of the Xiong'er terrane and the location of the Qiyugou gold deposit, modified after Lu et al. (2004).
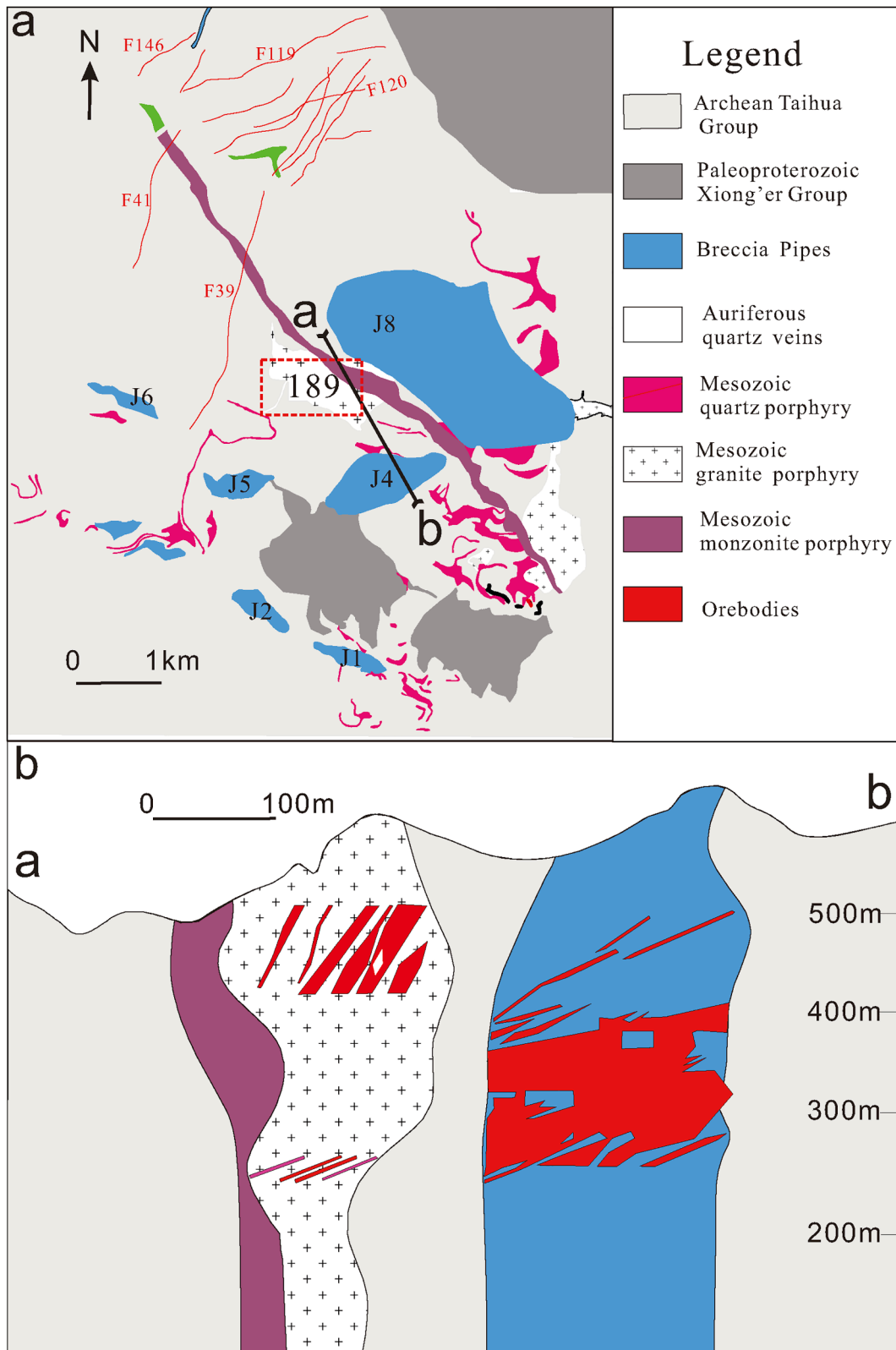
Fig. 2. (a) Geological map of the Qiyugou gold deposit and (b) No. 10 prospecting profile.

The Xiong'ershan gold area in the southern margin of the North China Craton is one of the largest gold districts in China, containing 20 ~ 30 major gold deposits, with gold reserves up to 300 tons (Mao et al. 2002). Some gold deposits in this area have a Bi-rich, As-poor signature (Wang et al., 2020), providing an ideal example to investigate the

formation of Au-Bi association in these deposit and the role of bismuth in gold mineralization. The Qiyugou Au deposit is one of the largest gold deposits in the area, and contains several auriferous breccia pipes that are spatially related to granite-porphyry in Qiyugou (Qi et al., 2019). Numerous geochronology and fluid inclusion studies are available on

Mineral \ Stage	K-feldspar-quatz	Quatz-pyrite	Gold-quatz-pyrite	Gold-sulfides	Quatz-carbonate
Quartze	▬▬▬▬▬				▬▬
K-feldspar	▬▬▬				
Pyrite	▬▬▬▬				
Chlorite		▬▬▬▬			
Emplectite		▬▬▬▬			
Sericite		▬▬▬▬			
Calcite					▬▬
Magnetite			▬▬		
Hematite			▬▬		
Pyrrhotite			▬▬		
Chalcopyrite			▬▬	▬▬	
Galena			▬▬	▬▬	
Sphalerite			▬▬	▬▬	
Covellite				▬ ▬ ▬	
Sphene			▬ ▬ ▬		
Bismuthinite			▬▬	▬▬	
Bi(Te, S)			▬▬	▬▬	
Aikinite				▬▬	
Lillianite			▬▬	▬▬	
Cosalite			▬▬	▬▬	
Gustavite			▬▬	▬▬	
Native Bi			▬▬		
Electrum				▬▬	
Gold			▬▬		
Cuprobismute				▬▬	

Fig. 3. Paragenetic sequence of minerals in the Qiyugou gold deposit.

the Qiyugou deposit and confirmed that the deposit was formed at ca. 125 Ma (Wang et al., 2001, 2020) and the ore-forming fluids were magmatic in origin (Chen et al., 2009; Fan et al., 2011; Guo et al., 2007; Li et al., 2012). Abundant Bi-minerals were also suggested to be closely associated with Au mineralization (Wang et al., 2020). However, the study on the mineralogy of ores, particularly the Bi-minerals, is still very limited. Thus physicochemical conditions and mechanisms of Au-mineralization remain poorly understood in this deposit. In such contribution, we study the different types of mineralization at the Qiyugou deposit with the focus on the relationship between Bi-minerals and Au mineralization. In-situ trace and major elemental compositions of different generations of pyrites were obtained to constrain the physicochemical conditions of the gold mineralization, consequently confirming that whether such a kind of gold metallogenic system has produced preferential conditions for liquid Bi precipitation and Au concentrations.

2. Geological background

The Qiyugou deposit is located in the Xiong'ershan area, which lies on the southern margin of the North China Craton (NCC) (Fig. 1a). Numerous gold deposits (>300 t Au) exist in this area with different occurrences, including breccia pipe-hosted (Qiyugou and Dianfang), and altered-type gold deposits (Shanggong, Gongyu, Kangshan, Qinggangping and Luyuangou) (Mao et al., 2002). The Xiong'ershan area is bounded by the Machaoying Fault to the south and the Luoning Fault to the northwest (Fig. 1b). This area is dominated by amphibolite-facies metamorphic rocks of the Late Archean to early Paleoproterozoic Taihua Group (2.5–2.3 Ga; Xue et al., 1996; Xu et al., 2009), which mainly

consists of felsic gneiss, TTG gneiss, migmatite, amphibolite, and metamorphosed supracrustal rocks intercalated with mafic to ultramafic rocks (Xu et al., 2009). The Taihua Group is unconformably overlain by intermediate to silicic volcanic rocks of the Paleoproterozoic Xiong'er Group (Chen et al., 2009; Mao et al., 2010; Fig. 1b). The Xiong'er Group formed in the period of 1.80–1.75 Ga (Zhao et al., 2004, 2009) mainly comprising basaltic andesite, andesite and minor dacitic-rhyolitic rocks (Zhao, 2000; Zhao et al., 2002).

During the Mesozoic and Cenozoic, thinning of the cratonic lithosphere generated abundant intrusions of calc-alkaline granitoid and lamprophyre in the Xiong'ershan area, such as the Huashan (132.0 ± 1.6 Ma; Mao et al., 2010) and Wuzhangshan plutons (156.8 ± 1.2 Ma; Mao et al., 2010) (Fig. 1b). A large number of important alkaline porphyry-related gold and molybdenite deposits have been discovered in the Xiong'ershan area, such as the Leimengou porphyry Mo deposit and the Qiyugou breccia pipes Au deposit (Mao et al., 2002).

3. Geology of the Qiyugou gold deposit

The Qiyugou gold deposit is situated in the south-central part of the Xiong'ershan area. The deposit is located on the southeast part of the Mesozoic Huashan granitic pluton and bounded with the Taocun-Mayuan fault. Strata at Qiyugou includes the Late Archean amphibolite facies metamorphic rocks and the Paleoproterozoic silicic volcanic rocks, which are overlain by Quaternary sediments. Porphyries exposed at the Qiyugou area include quartz-porphyry (ca. 165 Ma; Deng et al., 2014), granite-porphyry (ca. 130 Ma; Qi et al., 2019), and monzonite-porphyry (ca. 125 Ma; Qi et al., 2019). Previous studies suggested that these porphyries have a spatial–temporal relationship with Au
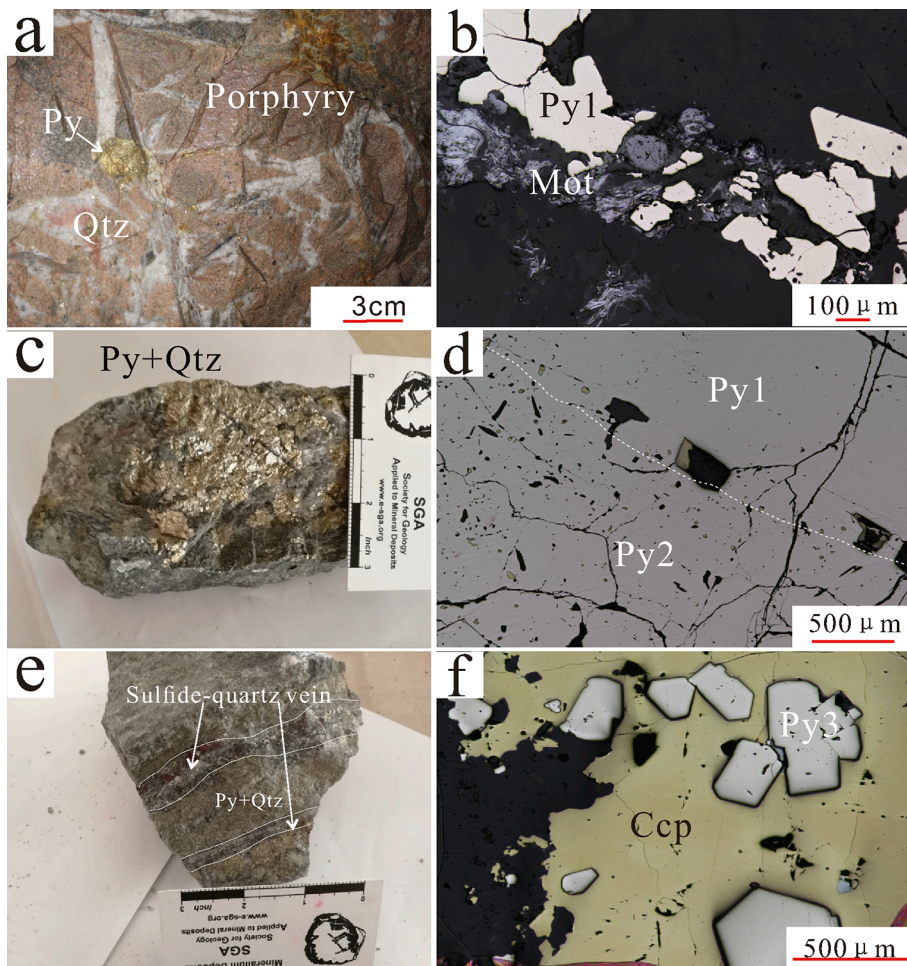
Fig. 4. Photographs (a, c, e) and reflected light photomicrographs (b, d, f) showing three generations of pyrite (Py1, Py2, and Py3) with different textures and morphologies. (a) Large crystals of the Py1 dispersed in milky quartz. (b) Py1 is coarse-grained subhedral crystals dispersing in quartz (c) The first and second generations of pyrite. (d) Py2 distributes around Py1 with abundant inclusions of sulfide mineral, native bismuth, and native gold in associated with light gray quartz. (e) (f) Py3 is intergrown with chalcopyrite and galena, characterized by medium- to fine-grained euhedral grains. Mineral abbreviations: Py pyrite, Qtz quartz, Ccp chalcopyrite.

mineralization (Chen et al., 2009; Mao et al., 2008; Yao et al., 2009). This deposit contains three types of ores, which are porphyry-, breccia- and quartz-vein-types, respectively. The total ore reserves of this deposit are approximately 70 t of gold (Mao et al., 2002) with ore grades ranging from 3 to 7 g/t (Chen et al., 2009).

The Au mineralization occurs in the porphyry complex of the central Qiyugou district and is named as No. 189 ore bodies (Fig. 2a). The mineralized zone is ~500 m long and ~100 m wide with a vertical thickness for over several hundred meters. The gold ore bodies mainly occur in the silicified core of porphyry bodies and can be divided into silicified and brecciated ore bodies. Breccia Au mineralization is the most important mineralization and distributes around No.189 ore-bodies (Fig. 2a). These breccia pipes are developed along NW-trending faults, resulted from NE-SW and NW-SE trending compression during the Mesozoic (Chen et al., 2009). The breccia mineralization, represented by J2, J4, J5, and J6 breccia pipes of ore bodies, mainly consists of massive pyrite and chalcopyrite that bear precious metals and cement breccias. Breccia is mainly sourced from rocks of the Taihua Group (60% ~ 80%) and metamorphosed volcanic rocks of the Xiong'er Group (40% ~ 20%) with latter occurring at the top of the breccia bodies. Granitic breccia, which were sourced from syenitic porphyry and granitic porphyry appeared in the middle and lower part of the breccia bodies. Additionally, quartz-vein-type gold ores also occur in the northwest of the Qiyugou gold deposit, bounded by NE-trending faults, which is considered as the distal products of porphyry mineralization (Shao, 1992). Along N-E trending faults, more than 70 gold-bearing veins have been discovered, and can be divided into three groups including NNE direction (such as F39 and F41), NE direction (such as F120 and F146), and NEE direction (such as F119 and F120) (150 ~ 2600 m length and

0.3 ~ 9.8 m width) (Fig. 2a). Although the occurrence of these three type of mineralization is very different, we found that their mineral assemblages are similar.

Based on mineral assemblages, the hydrothermal alteration, and the cross-cutting relationships, five stages of mineral precipitation are recognized (Fig. 3). Stage 1 is represented by milky quartz and K-feldspar, and stage 2 is dominated by milky quartz accompanied with coarse-grained, euhedral to subhedral "clean" pyrite (Fig. 4a, b). Stage 3 is characterized by light gray granular quartz and abundant medium-grained pyrite containing abundant bismuth mineral inclusions (Fig. 4c, d). Stage 4 is marked by a quartz-polymetallic sulfide assemblage consisting of pyrite, galena, chalcopyrite, and sphalerite (Fig. 4e, f). Stage 5 is composed of carbonate and quartz veins and traces of pyrite. Stages 3 and 4 are considered as the most important stages of gold deposition.

Pyrite is proved to be an important mineral hosting gold in the Qiyugou gold deposit, and has grain sizes highly variable from 100 μm to 30 mm and generally does not present clear compositional zonation under back-scatter electron images. Based on distinct morphology, textures, and paragenesis, three generations of pyrite, Py1, Py2, and Py3, were identified in Stages 2, 3, and 4, respectively (summarized in Fig. 3). Py1 with length of >1 mm occurs as coarse-grained subhedral crystals dispersing in milky quartz veins (Fig. 4a, b). This type of pyrite is devoid of any inclusions (Fig. 4b), but commonly disturbed by micro-fractures filled with quartz, chalcopyrite, galenobismutite, lillianite homologs, and galena. Py2 grains, generally overgrowing on Py1, are also associated with light gray quartz. Besides, they are coarse- to medium-grained (0.2 to 3 mm). Py2 grains differ from Py1 by abundant inclusions of sulfide minerals, native bismuth and native gold (Fig. 4c, d). Py3 is

Table 1
Individual LA-ICP analyses of pyrite grains.

Sample no.	Pyrite stage	Pb ppm	Co ppm	Ni ppm	Cu ppm	Zn ppm	As ppm	Ag ppm	Sb ppm	Au ppm	Bi ppm
QYG-7	Py1	–	5.52	14.0	0.02	–	0.41	–	–	–	–
QYG-7	Py1	3.19	2.28	5.39	0.23	0.10	1.32	0.05	–	0.03	1.26
QYG-7	Py1	–	40.1	25.7	0.08	0.12	1.68	–	–	–	–
QYG-7	Py1	425	124	7.56	16.3	1.70	2.84	5.27	0.09	0.38	39.0
QYG-13	Py1	–	2.50	1.05	0.02	0.18	10.8	–	–	–	–
QYG-13	Py1	1.32	20.4	21.0	0.18	0.09	7.23	0.02	0.01	0.02	1.51
QYG-17	Py1	0.61	2.33	95.5	0.08	0.08	18.8	0.03	–	–	0.83
QYG-18	Py1	2.76	0.05	40.0	0.19	0.20	3.57	0.03	0.02	0.02	3.46
QYG-18	Py1	0.09	64.6	32.7	0.25	1.54	3.30	0.03	–	–	0.64
QYG-18	Py1	1.23	283	38.5	0.10	0.10	4.50	–	–	–	0.09
QYG-18	Py1	0.02	447	174	0.12	0.11	1.40	0.03	0.01	–	0.15
QYG-18	Py1	0.11	406	406	0.15	0.76	2.61	0.01	0.02	–	0.36
QYG-38	Py1	2.89	317	67.6	0.55	0.11	10.0	0.67	–	–	3.44
QYG-38	Py1	0.61	716	34.2	0.07	0.18	0.75	–	0.03	–	0.11
QYG-38	Py1	3.45	9.38	6.98	0.10	0.11	0.44	0.29	0.01	–	1.28
QYG-38	Py1	0.03	443	333	0.29	0.16	8.40	–	–	–	0.02
QYG-38	Py1	0.01	148	74.2	1.01	0.32	2.12	–	0.02	–	–
QYG-38	Py1	0.01	283	249	0.66	1.17	6.78	–	–	–	–
QYG-37	Py1	621	87.5	6.11	3.15	0.13	28.7	17.3	0.07	0.23	51.2
QYG-37	Py1	26.6	219	73.2	0.54	0.09	2.39	1.84	0.01	–	6.85
QYG-37	Py1	1.68	204	0.47	0.06	0.05	247	–	0.03	0.02	0.40
QYG-37	Py1	9.95	0.37	0.13	0.27	0.24	3.81	0.45	0.02	–	16.2
QYG-37	Py1	55.3	2.03	0.08	1.24	15.8	6.26	0.07	0.05	0.02	2.04
QYG-37	Py1	567	300	106	7.91	0.45	3.57	12.8	0.04	0.23	69.5
QYG-37	Py1	634	267	105	7.25	0.28	4.99	9.87	0.14	0.23	70.9
QYG-28	Py2	6,341	117	1.69	50.0	10.0	66.3	80.5	0.01	0.08	181
QYG-5	Py2	28.2	0.13	0.68	126	7.55	40.3	2.76	0.04	0.22	32.0
QYG-5	Py2	0.06	0.32	0.32	0.00	0.07	11.6	0.01	–	–	0.07
QYG-5	Py2	5,130	606	0.14	7.05	0.08	10.7	114	0.86	0.30	4,635
QYG-22	Py2	20.4	86.6	58.3	27.2	0.26	176	0.99	0.02	0.03	12.7
QYG-22	Py2	2.14	143	15.6	1.97	0.10	1.65	0.39	–	0.10	23.4
QYG-22	Py2	0.83	127	157	15.9	0.12	0.20	0.12	–	0.03	3.00
QYG-22	Py2	238	141	27.5	510	1.88	52.3	51.3	0.12	0.33	720
QYG-22	Py2	14.634	98.6	62.9	0.12	0.15	1,483	0.71	–	0.09	2.21
QYG-22	Py2	10,100	744	114	59.9	0.15	1.36	1,265	3.12	0.37	10,758
QYG-3	Py2	176	196	209	84.0	2.99	2.86	35.7	0.38	0.18	18,587
QYG-3	Py2	46.8	5.27	12.9	0.49	0.16	0.20	1.73	–	0.06	40.2
QYG-3	Py2	14,751	2,437	209	333	0.89	7.80	1,340	6.65	0.05	14,913
QYG-3	Py2	594	305	388	68.7	0.64	10.7	60.9	0.03	2.03	474
QYG-3	Py2	172	377	210	224	2.73	3.32	10.3	0.23	0.19	10,134
QYG-32	Py2	12.8	23.1	20.3	0.43	0.50	17.2	0.45	0.01	0.04	20.7
QYG-32	Py2	26.8	6.90	16.3	113	12.4	17.0	2.99	0.01	0.06	33.1
QYG-17	Py2	45.6	31.7	17.7	7.20	1.95	5.21	1.42	0.03	0.15	72.2
QYG-18	Py2	11.7	58.0	18.1	85.3	2.48	4.13	1.89	0.04	1.38	39.1
QYG-18	Py2	6.47	299	46.5	833	55.9	18.8	12.3	0.07	1.06	43.0
QYG-18	Py2	4.75	95.7	420	0.76	3.97	8.84	0.27	0.00	0.04	6.52
QYG-18	Py2	10.9	96.7	184	0.48	0.48	5.28	0.08	0.05	0.05	9.62
QYG-18	Py2	2.53	30.0	28.9	174	12.0	5.92	1.53	–	0.13	8.67
QYG-18	Py2	3.44	20.0	14.9	0.20	0.32	4.46	0.09	0.01	–	7.84
QYG-18	Py2	79.5	32.1	58.1	224	15.9	10.9	4.40	0.02	0.32	52.8
QYG-18	Py2	0.12	36.5	118	0.34	0.17	8.86	0.01	–	–	0.54
QYG-37	Py2	1,849	209	27.2	20.3	0.35	29.3	47.7	2.02	1.31	360
QYG-38	Py2	56.1	139	1.92	29.1	0.10	15.6	24.3	0.13	28.9	32.2
QYG-38	Py2	415	41.2	18.7	22.0	0.53	0.12	17.6	0.01	0.05	40.0
QYG-38	Py2	15.6	232	5.35	0.31	0.17	0.48	0.64	0.01	0.04	11.3
QYG-38	Py2	20.5	5.16	6.42	1.53	0.04	5.08	0.32	0.14	0.05	7.60
QYG-38	Py2	6,695	198	25.2	36.8	22.9	1.51	79.9	0.22	0.05	171
QYG-5	py3	69.2	2.47	1.38	161	2.83	37.0	8.11	0.03	0.24	153
QYG-22	py3	8.87	437	58.7	137	0.27	0.92	0.97	0.01	0.04	2.63
QYG-22	py3	–	74.8	54.7	0.01	0.13	1.35	–	–	–	0.01
QYG −3	py3	0.10	24.2	657	0.12	0.13	40.8	0.01	0.01	–	0.24
QYG-38	Py3	0.01	390	22.6	0.07	0.15	0.96	–	0.01	–	0.02
QYG-38	Py3	4.26	49.7	43.8	432	6.07	4.76	3.81	–	0.77	14.1

– = Below the detection limit.

intergrown with chalcopyrite, galena, electrum and bismuthinite derivatives. The Py3 grains are euhedral and characterized by medium- to fine-grained sizes ranging from 0.1 to 0.5 mm (Fig. 4e, f). Only Py2 and Py3 grains are closely associated with gold mineralization.

4. Sampling and analytical methods

Representative ore samples were collected from the ore bodies at different levels in the Qiyugou gold deposit. In present study, fourteen samples (QYG-1, -2, -3, -5, -7, -13,-14, -16, -18, -22, -23, and -24) taken from breccia pipes, four samples (QYG-25, -28, -32, and -33) from No.189 ore body, and two samples (QYG-37 and QYG-38) collected from
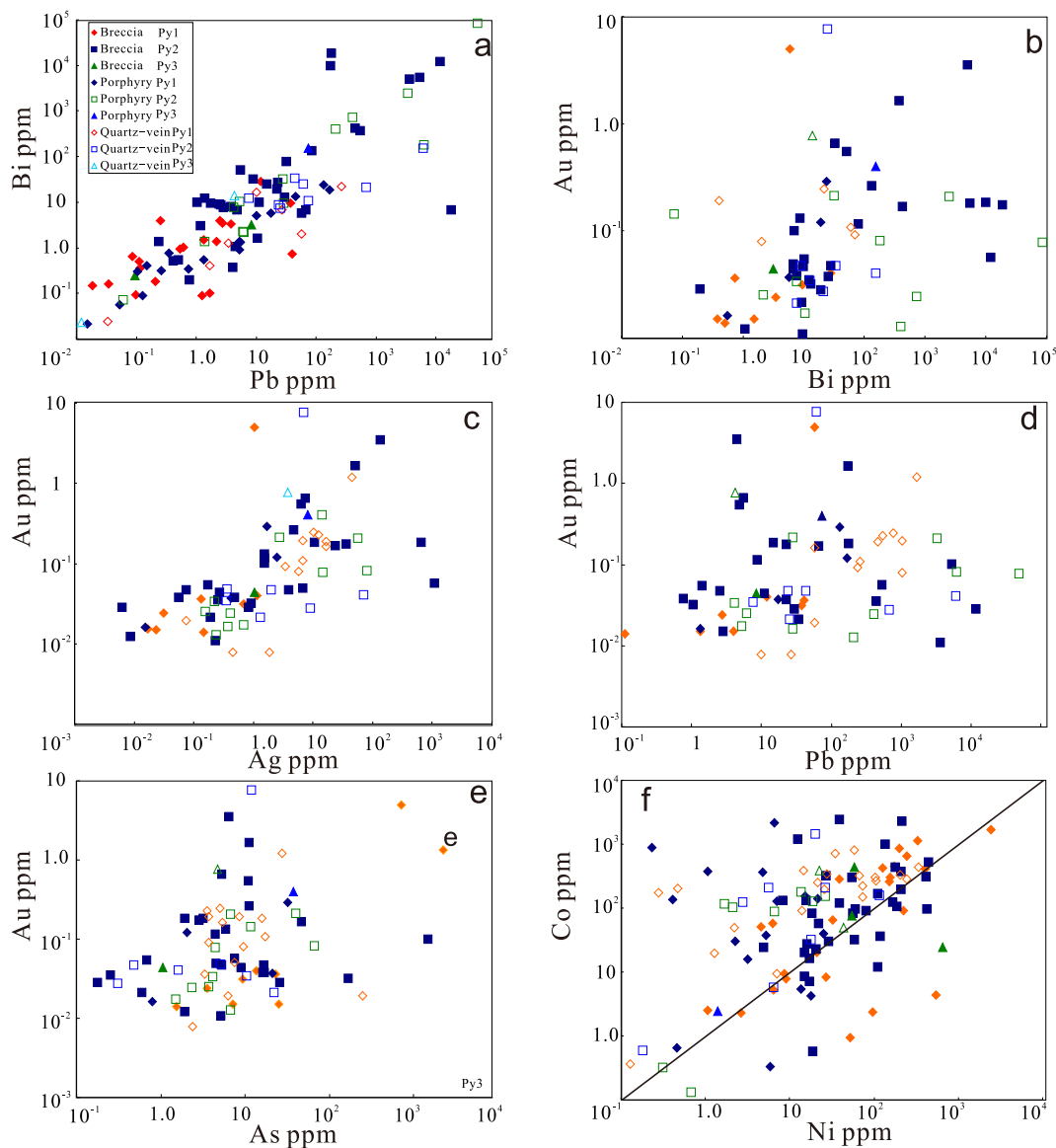
Fig. 5. Correlations between Au, Ag, Bi, As, Pb, Co, Ni for different generations of pyrite.

quartz-vein-type gold ores were selected. The selected samples were prepared as polished sections for electron microscopic, in situ electron probe and laser ablation-inductively coupled plasma-mass spectrometry (LA-ICP-MS) analyses.

Scanning Electron Microscope (SEM, SUPRA 55 SAPPHIRE, ZEISS Company, Germany) was used to investigate the bismuth mineral texture and semi-quantitative composition under the back-scattered electron (BSE) mode at the Guangzhou Institute of Geochemistry, Chinese Academy of Sciences. Major element compositions of the ore minerals were obtained by a JXA-8230 electron-probe micro-analyzer (EPMA) at the Institute of Geochemistry, Chinese Academy of Sciences. With a beam diameter 1 μm, peak counting time 20 s, and background counting time 10 s, the EMPA analyses were performed under an acceleration voltage 20 kV and a beam current 20 nA. Co^0 (for Co), FeS_2 (for S), Sb^0 (for Sb), FeAsS (for As), FeS_2 (Fe), Au^0 (for Au), Ni^0 (for Ni), $CuFeS_2$ (for Cu), ZnS (for Zn), FeS_2 (for S), Pb^0 (for Pb), Bi^0 (for Bi), Ag^0 (for Ag), Te^0 (for Te) and Se^0 (Se) were used as standards. Used X-ray lines and typical detection limits were listed as following: Ag (Lα, 0.03 wt%), As (Lα, 0.05 wt%), Au (Lα, 0.12 wt%), Bi (Mα, 0.12 wt%), Co (Kα, 0.03 wt%), Cu (Kα, 0.03 wt%), Fe (Kα, 0.02 wt%), Ni (Kα, 0.02 wt %), Pb (Mα, 0.10 wt%), S (Kα, 0.02 wt%), Sb (Lα, 0.03 wt%), Se (Lα,

0.03 wt%), Te (Lα, 0.04 wt%), and Zn (Kα, 0.04 wt%).

In addition, trace element concentrations in pyrite of different generations were measured by Laser Ablation Inductively-Coupled Plasma Mass Spectrometry (LA-ICP-MS) on polished thin sections at the In situ Mineral Geochemistry Lab, Ore deposit and Exploration Centre (ODEC), Hefei University of Technology, China. The analyses were carried out on an Agilent 7900 Quadrupole ICP-MS coupled to a Photon Machines Analyte HE 193-nm Ar-F Excimer Laser Ablation system equipped. A squid signal smoothing device is included in this laser ablation system. Helium was applied as a carrier gas. Argon was employed as the make-up gas and mixed with the carrier gas via a T-connector before entering the ICP (Wang et al., 2017). Each analysis was performed by a uniform spot size diameter of 30 mm at 8 Hz with energy of ~ 4 J/cm^2 for 40 s after measuring the gas blank for 20 s. The following basic set of isotopes for magnetite and hematite were monitored: ^{25}Mg, ^{27}Al, ^{29}Si, $^{43(44)}$Ca, ^{45}Sc, ^{49}Ti, ^{51}V, ^{53}Cr, ^{55}Mn, ^{57}Fe, ^{59}Co, ^{60}Ni, ^{65}Cu, ^{66}Zn, ^{71}Ga, ^{74}Ge, ^{88}Sr, ^{89}Y, ^{90}Zr, ^{93}Nb, ^{95}Mo, ^{97}Mo, ^{111}Cd, ^{115}In, ^{118}Sn, ^{137}Ba, ^{178}Hf, ^{181}Ta, ^{182}W, and ^{209}Bi. Multiple isotopes of Ca and Mo were measured to test for data consistency. The isotopes for ilvaite are ^{7}Li, ^{11}B, ^{23}Na, ^{25}Mg, ^{27}Al, ^{29}Si, ^{42}Ca, ^{45}Sc, ^{49}Ti, ^{51}V, ^{53}Cr, ^{55}Mn, ^{57}Fe, ^{59}Co, ^{60}Ni, ^{65}Cu, ^{66}Zn, ^{71}Ga, ^{74}Ge, ^{85}Rb, ^{88}Sr, ^{89}Y, ^{90}Zr, ^{93}Nb, ^{97}Mo, ^{109}Ag, ^{111}Cd, ^{118}Sn, ^{121}Sb,
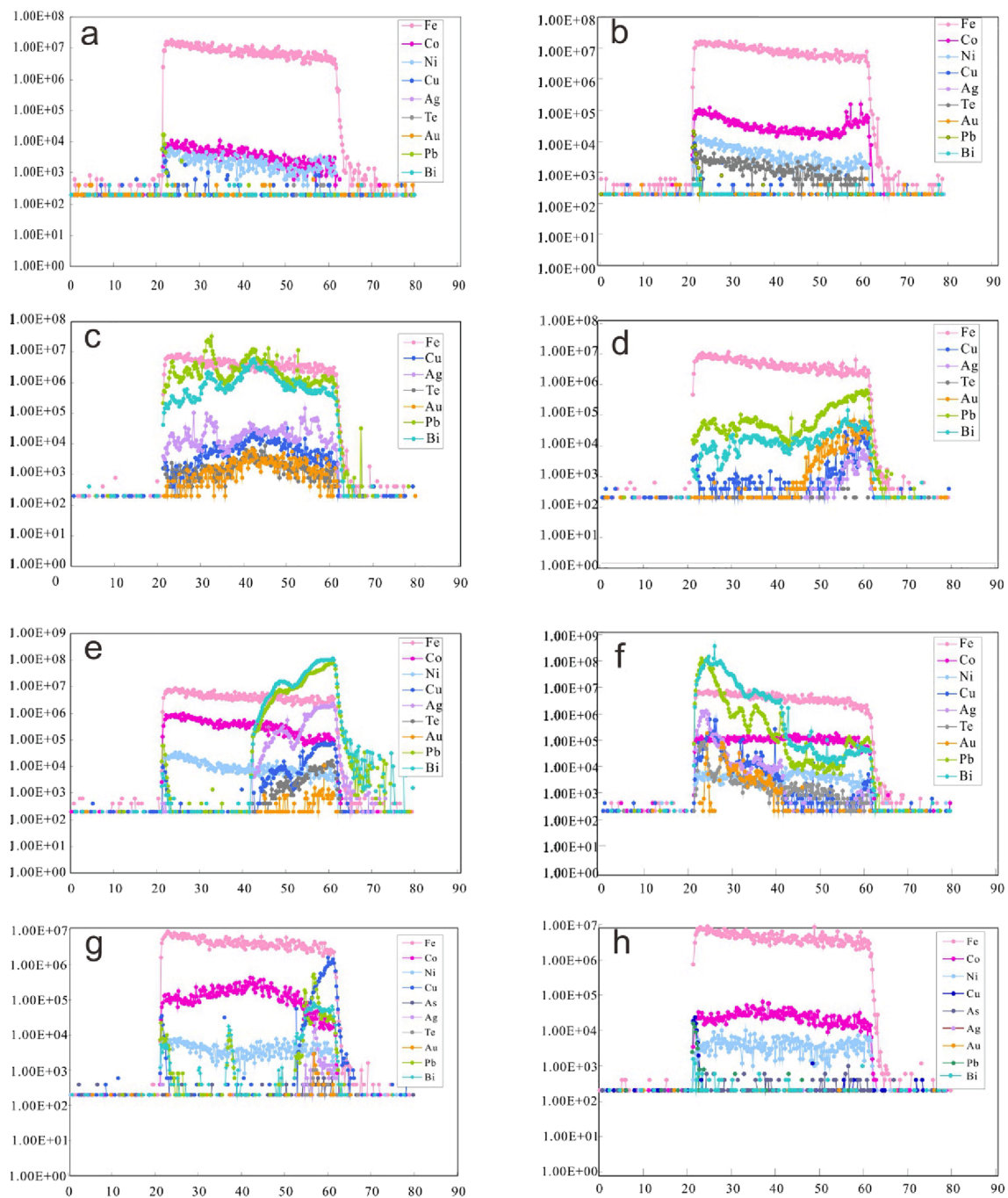
Fig. 6. Time-resolved LA-ICP-MS depth–concentration profiles (ion-signal intensity, counts per second) of Au, Ag, Te, Fe, Co, Ni, Cu, Pb, and Bi for pyrite grains of different generations from the Qiyugou gold deposit. (a-b) Py1 is depleted in most elements, like Pb, Zn, Cu, Ag, B, and Au. The time-resolved LA-ICP-MS depth profiles of Py2 (c-f) show a significant increase in Au, Pb and Bi signal intensities with sharp irregularities in other portions, indicating that some Py2 grains contain small amounts of invisible gold and bismuth minerals, occurring as microscopic inclusions or solid solutions. (h-i) The Py3 is similarly to Py1.

^{133}Cs, ^{137}Ba, ^{139}La, ^{140}Ce, ^{141}Pr, ^{146}Nd, ^{147}Sm, ^{153}Eu, ^{157}Gd, ^{159}Tb, ^{163}Dy, ^{165}Ho, ^{166}Er, ^{169}Tm, ^{172}Yb, ^{175}Lu, ^{178}Hf, ^{181}Ta, ^{182}W, ^{208}Pb, ^{209}Bi, ^{232}Th and ^{238}U. Data reduction was performed with 'ICPMSDataCal' software program (Liu et al., 2008) using ^{57}Fe determined by EPMA as the internal standard and SRM 610, BCR-2G, and MASS-1 as external standards in order to plot calibration curve. The preferred values of element concentrations for the USGS reference glasses are from the GeoReM database.

Previous studies have demonstrated that fugacity-fugacity diagrams are useful tools to predict the physicochemical conditions (e.g. fTe$_2$, fS$_2$ and fO$_2$) of ore formation (Afifi et al., 1988a, 1988b; Xu et al., 2014).

The detailed calculation methods of fugacities of S$_2$(g), Te$_2$(g) and O$_2$(g) have been shown in previous studies (Afifi et al., 1988a, 1988b; Simon et al., 1997; Xu et al., 2014). LogfO2 vs. pH diagrams at different temperature showing the areas of iron oxides can be used to estimate approximately oxygen fugacity. The thermodynanic databases are from SUPCR92 and SLOP98, and the diagram was drawn by the CHOSZ package of R (Dick, 2008).
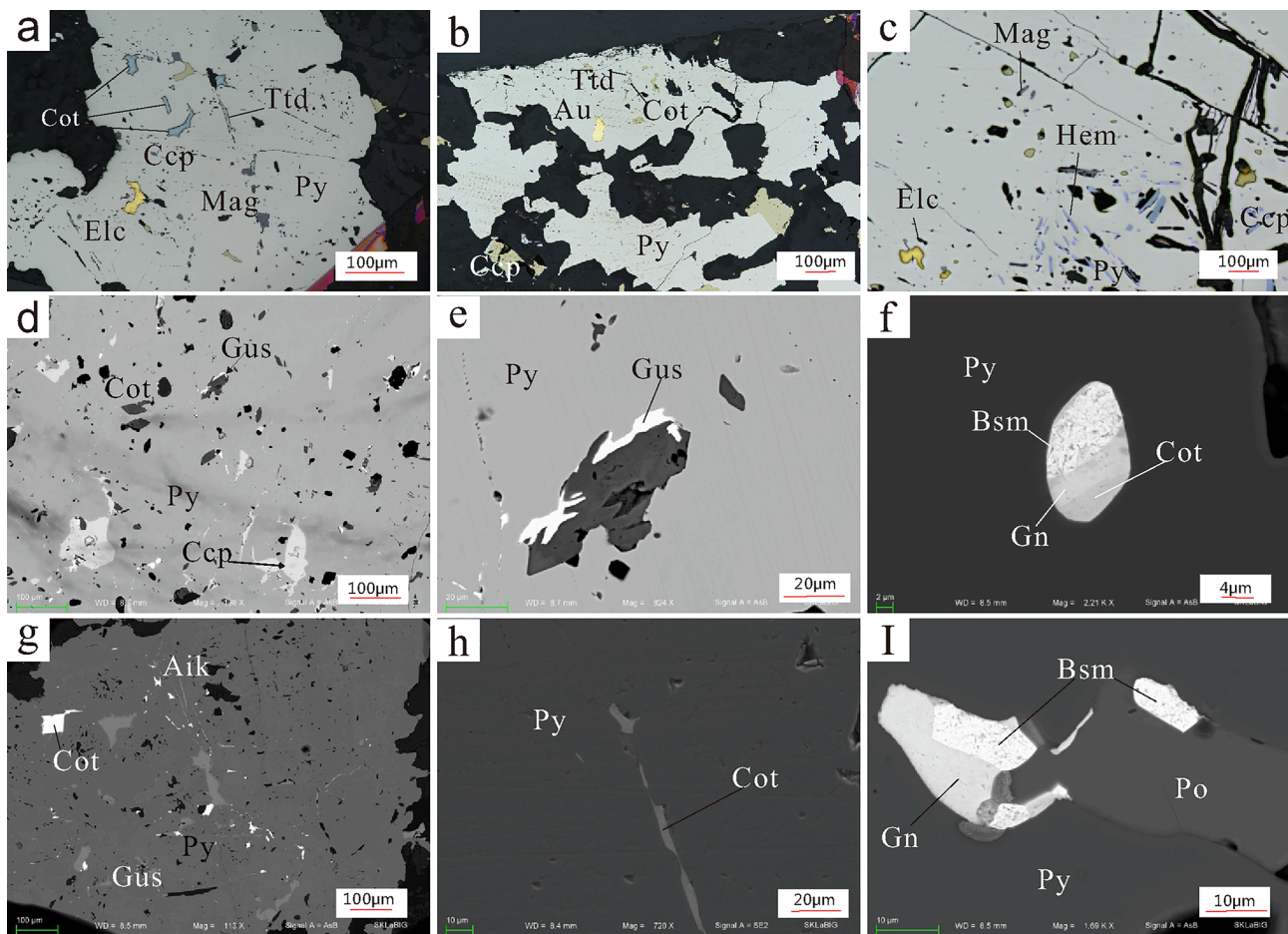
Fig. 7. Reflected-light photomicrographs of bismuth minerals assemblages from the Qiyugou gold deposit. (a-e, g-h) Tetradymite (Ttd), cosalite (Cot), magnetite (Mag), hematite (Hem), chalcopyrite (Ccp), electrum (Elc), gustavite (Gus), and native gold (Au) in pyrite (Py). (f) Bleds of native bismuth (Bsm), galena (Gn), and cosalite (Cot). (i) Bleds of native bismuth (Bsm) and galena (Gn) coexisting with pyrrhotite (Po). Figure. a, b, and c are reflected light microphotographs, while others are BSE images.

5. Result

5.1. LA-ICP-MS trace elements of pyrite

LA-ICP-MS data of totally 136 individual analytical spots of pyrites from the Qiyugou deposit are given in Table 1 and detailed data in Appendix table. The Py1 grains that formed during stage 2 are depleted in Pb, Zn, Cu, Ag, Bi, and Au elements. Only 19 of 70 analyses of Py1 reveal detectable gold, with values varying between below detection and 1.35 ppm and averaging in0.20 ppm. The Py2 grains are enriched in selected trace elements (Au, Ag, Cu, Pb, Bi) compared to Py1. The Au contents of the Py2 grains vary from below detection limit to 7.63 ppm, with an average of 0.96 ppm, and Pb varies from 0.24 ppm to 0.48 wt%, with an average of 1923 ppm, which is similar to Bi that varies from 0.99 ppm to 0.86 wt%, with an average of 2574 ppm. The wide range of Bi and Pb contents in Py2 and the positive correlation between Pb and Bi (Fig. 5a) are probably related to abundant micro-inclusions of Pb-Bi sulfosalt in the Py2, as observed in the thin sections (Fig. 7). The LA-ICP-MS trace elemental composition of Py3 is similar to Py1. The Au contents of Py3 range from below detection limit to 0.77 ppm, 0.35 ppm on average. Arsenic, which is generally considered to play essential role for incorporation of invisible gold in pyrite (Reich et al., 2005), is poor in the Qiyugou deposit and has no correlation with Au (Fig. 5e).

The time-resolved LA-ICP-MS depth profiles obtained from pyrite grains of different generations can be employed to illustrate the relative concentrations of Au, Ag, Bi, Pb, Te, and As and trace gold nanoparticles in the analyzed samples. Py1 and Py3 grains have Au, Ag, Te, Pb, and Bi signal intensities that are comparable to the respective background values (Fig. 6a, b, g, h). This suggests that these pyrite grains contain extremely little Au, Ag, Te, Pb, and Bi. In contrast, the time-resolved LA-ICP-MS depth profiles of Py2 grains show a significant increase in Au, Pb and Bi signal intensities with sharp irregularities in other portions, suggesting the overall presence of inclusions in the ablated material. Representative depth profiles are illustrated in Fig. 6c, d, e, f. Individual LA-ICP-MS spots have irregular depth profiles due to the gold and bismuth mineral inclusions of varying sizes and the time-resolved LA-ICP-MS depth profiles of Py2 grains preserve excellent correlation trends between Au and Bi.

5.2. Mineralogy and mineral chemistry of bismuth minerals

Numerous bismuth minerals have been recognized in the Qiyugou gold deposit, including cosalite, tetradymite, lillianite homologs, native bismuth, bismuthinite derivatives, and cuprobismutite homologs. These Bi-minerals are mostly shown in Stage 3 and 4, which contain different the assemblages of Bi-minerals assemblages show the difference. Stage 3 is dominated by coarse-grained pyrite containing chalcopyrite, galena, pyrrhotite, native-Bi, Ag-Pb-Bi ± Cu sulfosalts (members of the lillianite-homologous series), Pb-Bi sulfosalts, electrum, and native gold inclusions (Fig. 7). In contrast, Stage 4 comprises mainly chalcopyrite, pyrite, galena, bismuthinite, aikinite, magnetite, hematite, chlorite, epidotite, and electrum (Fig. 8). The characteristics of diverse Bi-minerals are described below. Their chemical compositions are shown in Tables 2, 3.
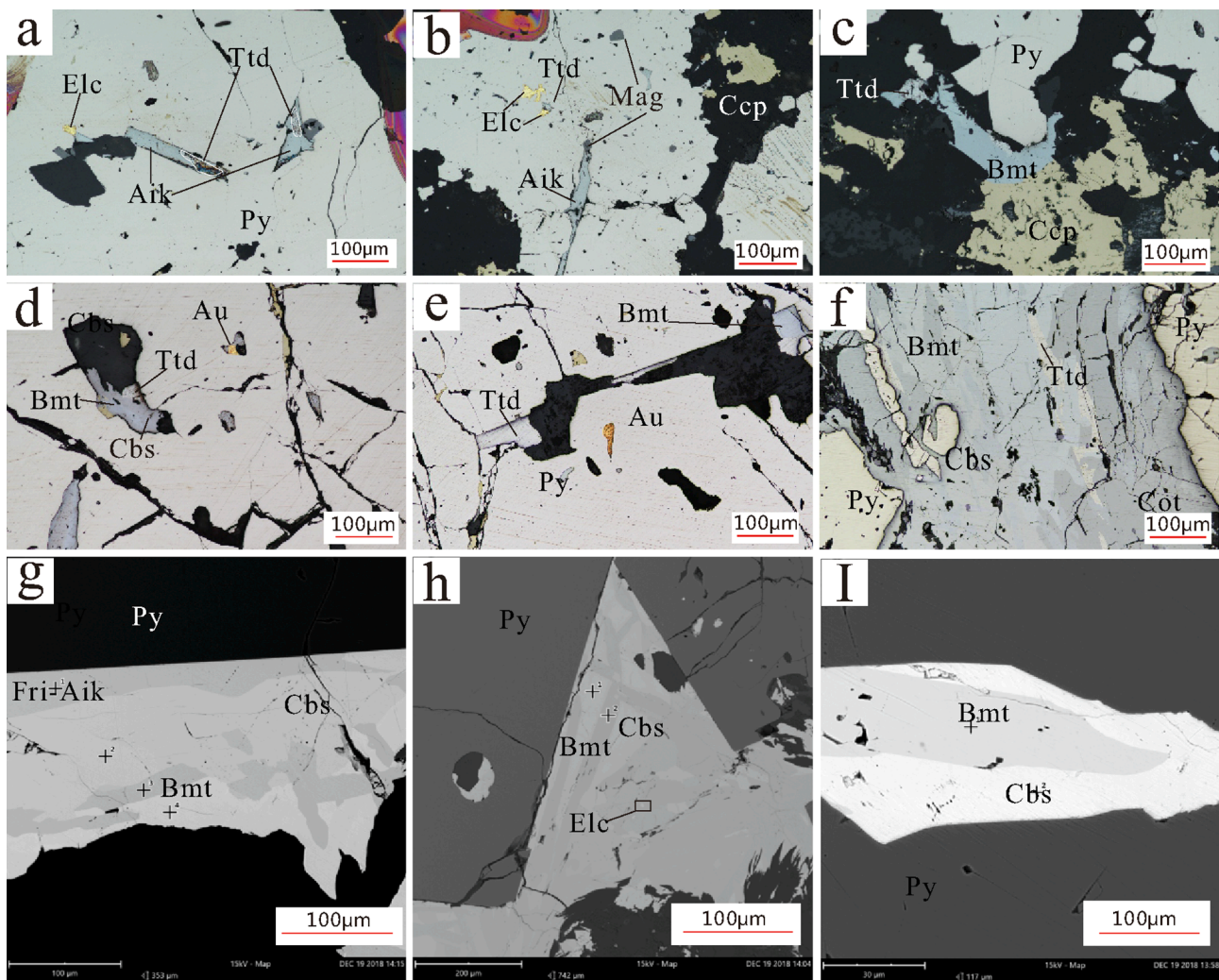
Fig. 8. Images of bismuth chalcogenides from the Qiyugou gold deposit. (a-b) Electrum (Elc), tetradymite (Ttd), and aikinite (Aik) occur as microfractures of Py2. (c) Bismuthinite (Bmt), tetradymite (Ttd), and chalcopyrite (Ccp) along the boundary of pyrite. (d) Bismuthinite (Bmt), tetradymite (Ttd), cuprobismutite (Cbs), and aikinite (Aik) as inclusions in pyrite. (e) Bismuthinite (Bmt), tetradymite (Ttd) along the boundary of pyrite and gold as tiny inclusion in pyrite. (f-i) Bi-sulfosalts (Bismuthinite, tetradymite, aikinite, cuprobismutite, and aikinite) filling the intergranular spaces of pyrite.

5.2.1. Pb-Bi sulfosalt

As shown in the Bi-(Ag + Cu)-Pb ternary diagram (Fig. 9), cosalite is the main Bi-Pb sulfosalts in the deposit (Fig. 7a, b, f, g, h). It occurs as irregular inclusions in pyrite and coexists with chalcopyrite, galena, lillianite-gustative, native bismuth, and native gold. Cosalite contains 42.6 ~ 45.2 wt% Bi, 31.8 ~ 36.0 wt% Pb, and 15.8 ~ 16.7 wt% S as well as trace amounts of Fe (<3.53 wt%), Cu (<4 wt%), and Ag (<2.15 wt%) (Table 3). The chemical composition of cosalite is calculated as $Bi_{7.90\sim7.99}(Pb_{6.68\sim7.22}Fe_{1.36\sim2.42})_{8.60\sim9.10}S_{18.91\sim19.50}$.

5.2.2. Pb-Bi-Ag sulfosalt

Lillianite homologs belong to the main type of Pb-Bi-Ag sulfosalts at the Qiyugou deposit (Fig. 7c, e). The ideal formula is proposed as $Pb_{N-1-2x}Bi_{2+x}Ag_xS_{N+2}$ (Makovicky and Karup-Møller, 1977). All these minerals generally contain Ag, Bi and Pb, while Cu, Sb and Te are below the detection limits in most cases (Table 3).

5.2.3. Native bismuth

Native bismuth occurs in the Qiyugou deposit as blebs intergrown with pyrrhotite and galena (Fig. 7f, i). It also occurs in contact with gold and Pb-Bi sulfosalts. EPMA results of native bismuth indicate the mineral contains ca. 97 wt% Bi and ca. 3.6 wt% of Fe (Table 2).

5.2.4. Bismuthinite derivatives

Bi-Cu-Pb sulfosalts are abundant in the Qiyugou deposit and belong to the bismuthinite derivatives, which are an isomorphic series with the two end members of bismuthinite (Bi_4S_6) and aikinite ($Cu_2Pb_2Bi_2S_6$) (Fig. 8). Besides, they are usually shown as micro-fracture infillings or intergranular phases of pyrite coexisting with chalcopyrite, galena, electrum, and tetradymite. Compositionally, bismuthinite includes ca. 77 wt% Bi and ca. 20 wt% S, with small amounts of Cu (1.13 ~ 2.34 wt%) and Fe (<1.14 wt%) (Table 3). The average composition of bismuthinite can be formulated as $Bi_{7.61\sim7.82}(Cu_{0.35\sim0.74}Fe_{0\sim0.12})S_{11.75\sim12.41}$. Based on the substitution mechanism of $Pb^{2+} + Cu^{1+} = Bi^{3+}$, the generalized formula of bismuthinite derivative is given as $Cu_xPb_yBi_{8-1/2(x+y)}S_{12}$, where x should be equal or very similar to y. The SEM data of bismuthinite derivatives from the Qiyugou gold deposit is shown in Table 3, which can be plotted in the Bi-Cu-Pb ternary diagram (Fig. 10).

5.2.5. Cu-Bi sulfosalt

Cuprobismute homologues are present as acicular blades in the microfracure and intergranular of pyrite. Cuprobismute homologues from the Qiyugou deposit contain ca. 66.2 wt% Bi, ca.12.9 wt% Cu, and ca. 18.7 wt% S, with minor amounts of Fe (ca. 0.53 wt%) and Ag(ca. 1.1 wt%) (Table 2; Fig. 8d, f, g, h, i).

Table 2
Electron microprobe data of visible gold, native bismuth and Bi-chalcogenide in the Qiyugou gold deposit.

	Au	Fe	Bi	Se	Co	Te	Ni	Ag	Cu	Pb	Zn	S	Total	Au/(Au + Ag)
Gold														
QYG-1	76.04	1.29	0.85	0.02	–	–	0.00	21.05	–	–	0.26	0.26	99.67	0.78
QYG-3	76.21	3.61	1.25	0.01	–	0.08	–	19.09	0.01	–	–	0.36	100.61	0.80
QYG-3	80.21	0.13	0.85	0.31	–	–	0.01	15.09	–	–	0.22	0.25	100.77	0.84
QYG-14	89.25	0.09	0.87	–	–	–	–	10.12	–	–	–	–	100.33	0.90
QYG-22	89.91	0.58	0.97	0.26	–	–	0.01	7.43	–	–	0.19	0.20	98.98	0.92
QYG-16	90.01	1.35	1.39	–	–	0.01	0.01	7.87	0.01	–	0.01	0.04	100.72	0.92
QYG-17	92.57	1.58	0.98	0.19	–	–	0.01	4.85	–	–	0.25	0.26	98.96	0.95
QYG-18	92.87	–	0.96	0.20	0.01	–	0.01	2.50	–	–	0.03	0.29	98.52	0.97
QYG-17	93.73	0.71	0.98	0.16	–	–	–	3.07	–	–	0.20	0.20	97.61	0.97
QYG-22	93.90	0.98	1.46	0.03	–	–	0.01	3.56	0.04	–	0.02	0.06	100.06	0.96
QYG-22	94.01	0.48	0.97	0.06	0.01	–	–	2.75	–	–	0.23	0.19	99.31	0.97
QYG-22	95.38	1.03	0.93	–	–	0.00	–	3.13	–	–	–	0.03	100.50	0.97
QYG-22	95.91	0.05	0.95	–	–	0.00	–	3.57	–	–	–	–	100.47	0.96
QYG-25	96.63	0.40	0.90	–	–	–	–	2.63	–	–	–	0.05	100.63	0.97
Native bismuth														
QYG-32	–	3.49	96.26	–	–	–	–	–	–	–	–	–	99.75	
QYG-32	–	5.21	94.53	–	–	–	–	–	–	–	–	–	99.74	
QYG-33	–	2.04	97.55	–	–	–	–	–	–	–	–	–	99.59	
QYG-24	–	3.08	95.98	–	–	–	–	–	–	–	–	–	99.07	
QYG-25	–	3.02	96.34	0.20	–	–	–	–	0.05	–	–	0.61	100.22	
Bi-chalcogenides														
QYG-25		0.23	59.52			35.00		0.10	0.05	–	0.04	4.72	99.65	
QYG-25		0.06	59.28			34.36		0.11	–	–	0.08	4.61	98.50	
QYG-32		0.06	58.70			34.62		0.12	0.02	–	0.06	4.66	98.24	
QYG-32		0.37	53.04			41.96		0.01	0.06	–	–	4.61	100.04	
QYG-33	–	1.44	54.43			38.28		0.05	0.01	–	0.05	4.26	98.51	

– Below the detection limit.

5.2.6. Bi-chalcogenides

In most case, bismuth chalcogenides are present as irregular inclusions or microfracture infillings in pyrite intergrown with chalcopyrite, galena, lillianite-gustative, native bismuth, bismuthinite derivatives, electrum and native gold (Figs. 7, 8). Tetradymite (Fig. 11) represented by formula $Bi_{1.73\sim2.03}Te_{1.92\sim2.2}S_{0.92\sim1.03}$, containS ca. 57.0 wt% Bi, ca.37.0 wt% Te, ca. 4.6 wt% S, and trace amounts of Fe (<0.08 wt%) and Cu (<0.054 wt%).

5.2.7. Native gold and electrum

Visible gold (native gold or electrum) is mainly hosted by pyrite as an infill of microfractures or inclusions (1 ~ 100 μm) (Fig. 12). In the meanwhile, chalcopyrite or quartz is also an important host for gold in the Qiyugou deposit. At stage 3, gold occurs as small blebs within pyrite, coexisting with chalcopyrite, galena, Bi-Pb sulfosalts, Ag-Pb-Bi sulfosalts (Fig. 12a, b, c, d, e). Visible gold has a high number in Au fineness (i.e., Au/ (Au + Ag)*1000), ranging from 841 to 982, 950 on average (Table 2), with smaller amounts of Fe (<1.58 wt%) and Bi (0.85 and 1.45 wt%). The gold of Stage 4 is shown as electrum locating in microfracture infillings or intergranular among pyrite grains, intergrown with bismuthinite derivatives, Bi-Cu sulfosalts, chalcopyrite, galena, and tetradymite (Fig. 12f, g, h, i). The Au fineness of electrum ranges from 783 to 898, 832 on average. In addition, it also contains minor amounts of Fe (0.09 ~ 1.29 wt%) and Bi (0.83 ~ 0.86 wt%).

6. Discussion

6.1. Formation conditions of bismuthide in different stages

A large number of bismuth minerals that coexist with gold have been found in the Qiyugou gold deposit, which can be divided into two groups based on the textural relationships and mineral assemblages. According to our result, Py1 grains of Stage 2 are free of any inclusions of bismuth minerals or gold, whereas Py2 of Stage 3 has abundant bled-like inclusions of native bismuth, pyrrhotite, native gold, lillianite homologues, Pb-Bi sulfosalt (galeobismutite and cosalite), and tetradymite,

indicating a decrease in fS_2, fO_2 and increase in fTe_2. Obviously, Py3 of Stage 4 is associated with chalcopyrite, galena, bismuthinite derivatives (bismuthinite and aikinite), tetradymite, and electrum, indicative of high fS_2 conditions. The absence of Au-tellurides in this stage indicates that fTe_2 was too low to reach the stability field of $AuTe_2$ (calaverite).

Previous studies demonstrated that Bi-Te minerals can record the physicochemical conditions (e.g. fTe_2 and fS_2) of ore formation (Afifi et al., 1988a, 1988b; Cepedal et al., 2006). Microthermometric measurements of primary fluid inclusions revealed that the temperatures of gold mineralization in the Qiyugou deposit range from 310 ~ 390 °C (stage 2, stage 3) and 200 ~ 289 °C (stage 4), respectively (Fan et al., 2011; Li et al., 2012), consistent with the formation temperature of bismuthide in various gold deposits elsewhere (Bi et al., 2011; Chapman et al., 2017; Ciobanu et al., 2004; Zhou et al., 2017). According to the Pb-Bi-Au-Ag-Te assemblages, we adopt the logfTe_2 versus logfS_2 diagram at 300 °C and 250 °C to evaluate Te and S fugacities for the deposition of sulfides and tellurides (Fig. 13). In stage 3, fTe_2 can be defined by $2Bi + 1.5Te_2(g) = Bi_2Te_3$ (300 °C), at ca. 10^{-11} (Xu et al., 2014). In the stage 4, the absence of calaverite indicate that the logfTe_2 (g) should be below the Au-$AuTe_2$ buffer. According to the phase's equilibrium of Bi_2S_3-Bi_2Te_3, the fTe_2 can be constrained between 10^{-11} and 10^{-9}. At stage 3, the coexisting pyrite and pyrrhotite suggests fS_2 values of 10^{-11} to 10^{-12}. An increase of S fugacity and decrease of temperature in Stage 4, which contributed to the precipitation of bismuthinite derivatives + tetradymite + magnetite + hematite + pyrite, suggests the estimated fS_2 of this stage is 10^{-10} to 10^{-11}. Meanwhile, the Bi-Te-S minerals (tetradymite) are characterized by low Bi/(Te + S) ratios of ≤1, implying that gold has precipitated under oxidizing conditions (Ciobanu et al., 2010). The pH value of the Qiyugou gold deposit was 6.34 at the Stage 1 and the ore-forming hydrothermal fluids transform from weakly acidic to weakly basicity during the ore-forming process (Shao, 1992). Base on the mineral assemblages, we adopt the logfO_2 versus pH diagram at 400 °C(Stage 2), 300 °C(Stage 3) and 250 °C(Stage 4) (Fan et al., 2011; Li et al., 2012) to evaluate oxygen fugacities for the Qiyugou gold deposit (Dick, 2008). The oxygen fugacity ranged from 10^{-26} to 10^{-23} at the Stage 2, while the oxygen

Table 3
Representative SEM data of Bismuth-sulfosalts from the Qiyugou gold deposit.

|	Fe	Bi	Ag	Cu	Pb	S	Au	Total
Lillianite-gustative								
QYG-3	2.52	35.48	3.01	–	42.74	15.59	–	99.34
QYG-5	3.05	35.51	–	–	45.67	15.78	–	100.01
QYG-5	3.38	36.45	–	–	44.06	16.11	–	100.00
QYG-6	1.90	36.98	–	–	44.90	16.23	–	100.01
QYG-13	1.39	35.68	2.28	–	44.65	16.01	–	100.01
QYG-13	2.33	48.86	9.46	–	22.70	16.64	–	99.99
QYG-13	3.12	37.56	4.11	–	42.60	13.56	–	100.95
QYG-14	4.84	35.11	3.15	–	39.96	16.93	–	99.99
QYG-14	1.98	44.43	4.97	2.45	30.13	16.07	–	100.03
QYG-14	1.98	46.99	5.73	1.98	26.38	16.55	–	99.61
QYG-15	1.65	44.95	6.55	6.56	23.66	16.64	–	100.01
QYG-15	2.15	48.11	6.15	1.35	25.25	16.29	–	99.30
Cosalite								
QYG-22	3.53	43.42	–	–	36.03	15.76	–	98.74
QYG-3	1.96	42.21	–	–	38.23	15.96	–	98.36
QYG-7	0.54	45.24	2.15	4.05	31.80	16.77	–	100.55
QYG-8	1.34	42.62	–	3.52	36.02	16.51	–	100.00
Bismuthinite derivatives								
QYG-22	0.70	32.92	–	10.50	38.79	17.09	–	99.30
QYG-22	0.59	32.92	–	10.86	38.81	16.83	–	99.42
QYG-3	–	33.25	–	11.06	39.12	16.57	–	100.00
QYG-3	1.32	34.22	–	10.45	37.09	16.91	–	98.67
QYG-3	–	36.81	–	10.04	36.81	16.67	–	100.33
QYG-32	1.01	44.23	–	7.86	30.13	16.77	–	98.99
QYG-32	1.01	44.23	–	7.86	30.13	16.77	–	98.99
QYG-16	0.54	45.24	2.15	4.05	31.80	16.77	–	100.01
QYG-17	1.30	57.20	–	4.75	19.38	16.87	–	98.20
QYG-17	–	57.31	–	4.87	20.23	17.57	–	99.98
QYG-18	–	58.08	–	4.86	19.33	17.35	–	99.62
QYG-19	0.52	58.16	–	4.32	19.24	17.40	–	99.12
QYG-19	0.52	58.16	–	4.32	19.24	17.40	–	99.12
QYG-21	1.14	59.10	–	4.12	17.85	17.50	–	98.57
QYG-21	1.14	59.10	–	4.12	17.85	17.50	–	98.57
QYG-21	–	76.87	–	2.19	–	20.65	–	99.71
QYG-22	–	76.87	–	2.19	–	20.65	–	99.71
QYG-22	0.30	77.66	0.01	1.36	0.00	18.81	0.03	98.26
QYG-22	–	77.83	–	1.41	–	20.67	–	99.91
QYG-25	–	77.88	–	1.09	–	19.98	–	98.95
QYG-25	–	77.88	–	1.09	–	19.98	–	98.95
QYG-25	–	77.93	–	1.47	–	20.67	–	100.07
QYG-25	–	78.12	–	1.28	–	20.17	–	99.57
QYG-26	0.02	79.02	0.00	1.15	0.00	18.08	0.00	98.75
Cuprobismute homologues								
QYG-15		67.53	1.29	12.97	0.00	18.84	0.00	100.62
QYG-15		66.36	1.06	12.97	0.00	18.82	0.00	99.21
QYG-15		66.49	1.03	13.08	0.00	18.80	0.00	99.41
QYG-25		66.50	1.05	13.26	0.00	18.69	0.00	99.50

– = Below the detection limit.
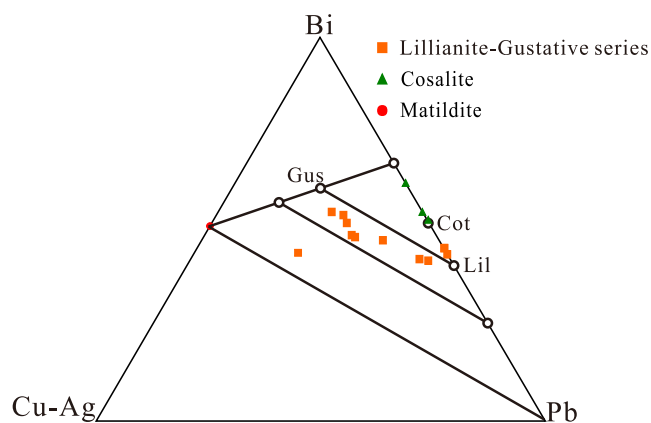
Fig. 9. Ternary diagram of Bi–Pb and Bi–Pb–Ag sulfosalts from the Qiyugou deposit.

fugacity ranged from 10^{-30} to 10^{-36} at the Stage 3 and Stage 4 (Fig. 14), suggesting that the oxygen fugacity decreased from the early stage to the main stage.

6.2. Gold scavenging by Bi melt

Our new results show that gold in the Qiyugou gold deposit almost presents as visible (native gold and electrum) (Fig. 12) and small amounts of invisible gold in pyrite. LA-ICP-MS depth profiles for Au, Ag, Pb and Bi are generally ragged and show parallel trends, suggesting that the invisible gold may be present as nano-scale native gold and associated with Pb-Bi-Ag-Cu mineral inclusions in pyrite (Fig. 6). Visible gold (native gold or electrum) is mainly hosted by pyrite as an infill of microfractures or inclusions, coexisting with Bi-Pb sulfosalts, Ag-Pb-Bi sulfosalts, bismuthinite derivatives, Bi-Cu sulfosalts, chalcopyrite, galena, and tetradymite (Fig. 12). Moverover, mineral assemblages suggest that gold was deposited under low Te fugacity (fTe$_2$) condition (fTe$_2 \sim 10^{-11}$(stage 3) and fTe$_2 \sim 10^{-9}$ to 10^{-11}(stage 4)), which is far less than that of conditions, where tellurium can sever as important gold
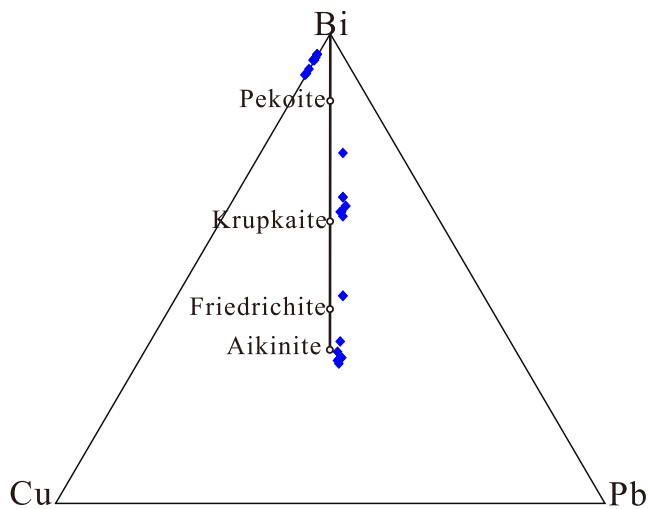
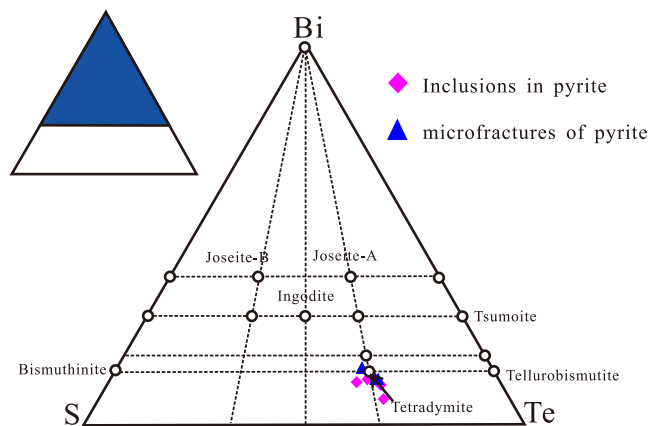**Fig. 10.** Ternary plot of bismuthate derivatives from the Qiyugou deposit.

Fig. 11. Ternary plot (Bi + Pb)-Te-(S + Se) of tetradymite and the unnamed BiTeS from the Qiyugou deposit. (Modified after Cook et al. (2009b)).

scavengers (fTe$_2 \sim 10^{-6.8} \sim 10^{-10.8}$, Bi et al., 2011; fTe$_2 \sim 10^{-7.9}$, Meng et al., 2020). Arsenic is also poor in the Qiyugou deposit and has no correlation with Au (Fig. 5e). These features further suggest that Au enrichment was mainly controlled by Bi, rather than As or Te, a scenario demonstrated in various gold deposits elsewhere (Meng et al., 2020; Reich et al., 2005; Zhang and Spay, 1994).

Tooth et al. (2011) found that liquid bismuth from hydrothermal fluids is able to be formed from fluid-rock or fluid–fluid reactions. In favorable sulfur-oxygen fugacities and temperatures (above 271 °C), Bi melts can scavenge Au from hydrothermal fluid, which can form economic gold deposits from Au-undersaturated aqueous fluids (Tooth et al., 2008). This mechanism is regarded as liquid bismuth collector model, which has been applied to various hydrothermal deposits (Acosta-Góngora et al., 2015; Cockerton and Tomkins, 2012; Cook and Ciobanu, 2004; Oberthür and Weiser, 2008; Törmänen and Koski, 2005; Zhou et al., 2016). In the case of the Qiyugou deposit, the mineralization temperatures (250–390 °C) obtained from fluid-inclusion thermometry (Fan et al., 2011; Li et al., 2012) exceed the low melting points of the Au-Bi phases (Okamoto and Massalski, 1983), implying that bismuth would have been present as liquids or melt droplets. In hydrothermal fluids, bismuth exists mainly as Bi(OH)$_3$(aq) complex, and is subsequently reduced to Bi^0 with electrons donated by graphite or pyrrhotite, causing the precipitation of Bi melt droplets (Törmänen et al., 2005; Tooth et al., 2008).

Pyrrhotite inclusions in Py2 commonly coexist with native bismuth,

Bi-bearing minerals, and native gold (Fig. 7f, h) at stage 3 in the Qiyugou deposit. Therefore, Bi^{3+} in the fluid transforms to be Bi^0 liquid via the following reaction (1):

$$9FeS + 6H_2O + 2Bi(OH)_3 \text{ (aq)} = 2Bi(Liq) + 3Fe_3O_4(s) + 9H_2S(aq) \quad (1)$$
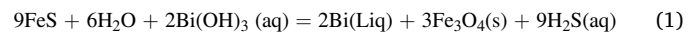
At Stage 4, the brittle-ductile deformation of early pyrite was followed by formation of a large number of polymetallic sulfides along the developed fissures in the pyrite mainly including chalcopyrite, galena, silver-gold ore, magnetite and a small amount of hematite. Because Fe is predominantly present as Fe^{2+} in hydrothermal fluids (Brugger et al., 2016), the precipitation of Fe^{3+}-bearing minerals is an oxidation reaction, which results in the precipitation of liquid bismuth, presented as follows:

$$2Bi^{3+}(aq) + 9Fe^{2+}(aq) + 12H_2O = 3Fe_3O_4 + 2Bi(Liq) + 24H^+ \quad (2)$$

$$4Au(HS)^{2-}(aq) + 4H^+ + 2H_2O = 4Au^0 \text{ (in Bi Liq)} + 8H_2S(aq) + O_2(g) \quad (3)$$
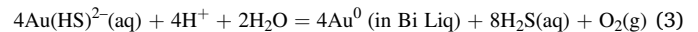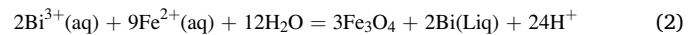
Bi melts can scavenge Au from the Au-undersaturated hydrothermal fluids (reaction 3), forming Bi-Au melts (Tooth et al., 2011). However, the Au in the Qiyugou gold deposit occurs mostly as native particles with minor shown as Bi-Au alloys. Zhou et al., (2018) speculated that some Bi were likely to be re-dissolved or altered in the fluid, leaving behind gold, through the following two processes: 1) production of Bi-melts from hydrothermal fluids and scavenging Au from the hydrothermal fluids and 2) convert of stable native bismuth to bismuthinite or Pb-Bi-Te-S minerals as a result of Bi sulfidation reactions triggered by decreasing temperature or increasing sulfur contents.

In summary, our new findings on Bi-minerals allow us to propose a new model for the origin of the Qiyugou deposit. In the quartz-gold-pyrite stage (Stage 3), gold mainly exists as inclusions in pyrite, where it coexists with natural bismuth, pyrrhotite and bismuth minerals. Accompanied with scavenges of Au from the hydrothermal fluids decreases in fO$_2$ and temperature triggered the precipitation of native Bi. Sulfidation reactions of the Bi melt would also release Au back into the hydrothermal fluids that converted Bi melt into bismuth minerals and native Au (Ciobanu et al., 2010). Subsequently, the bismuth minerals and native Au were subsequently incorporated into pyrite as inclusions. In the polymetallic sulfide stage (stage4), decreasing temperatures, and increasing sulfur contents also maintained the stabilization of bismuthinite (Tooth et al., 2011). Sulfidation driven by cooling or increasing sulfur contents results in the transformation of the Au-Bi liquid into a stable assemblage of native gold and bismuthinite (Tooth et al., 2011). Hence, this study shows that the mineralization of Au in the Qiyugou gold deposit is the result of Au concentration via the liquid bismuth collector model and emphasizes that bismuth can be important ore-controlling element in gold deposits related to magmatism, and is of great significance for ore prospecting in the region.

7. Conclusion

1) Gold in the Qiyugou gold deposit mostly occurs as visible gold (native gold and electrum) and small amounts of invisible gold in pyrite. LA-ICP-MS depth profiles suggest that the invisible gold in Qiyugou deposit presents as nano-scale, submicroscopic inclusions of native gold or electrum.
2) Gold precipitation in Stages 3 and 4 appeared at the conditions of fTe$_2 = \sim10^{-11}$ and fS$_2 = \sim10^{-11}$ to 10^{-12}, and fTe$_2 = \sim10^{-9}$ to 10^{-11} and fS$_2 = \sim10^{-10}$ to 10^{-11}, respectively.
3) The decreases in fO$_2$ and temperature triggered the precipitation of liquid bismuth, and drove the scavenging of Au from the hydrothermal fluids. Moreover, our new findings emphasize that the formation of the Qiyugou gold deposits involved Au scavenging by Bi melt (i.e., Stages 3 and stage 4).
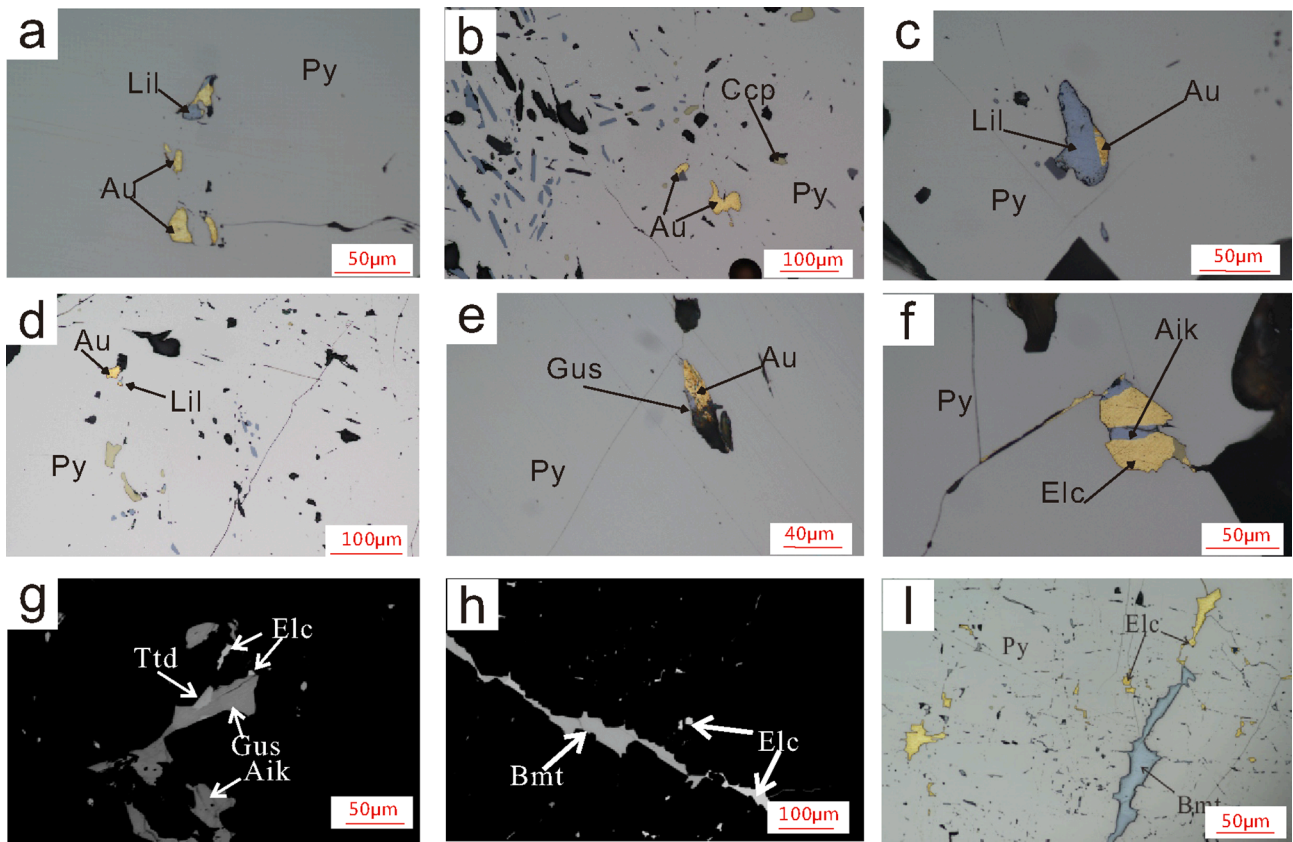
Fig. 12. Images of Au from the Qiyugou gold deposit. (a-e) Native gold(Au), gustavite(Gus), as inclusions in pyrite (Py) (f ~ i) Electrum (Elc),bismuthinite (Bmt), tetradymite (Ttd), and aikinite (Aik) occur as microfractures of Py.
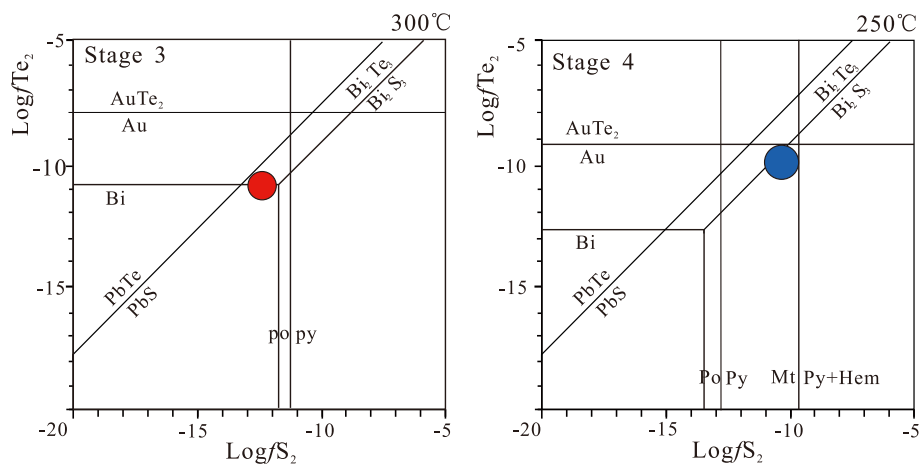

Fig. 13. Stability diagrams of log$f$S$_2$ and log$f$Te$_2$ for tellurides and sulfides at 300 °C and 250 °C (modified after Afifi et al., 1988a), as a function of fS$_2$ and fTe$_2$.
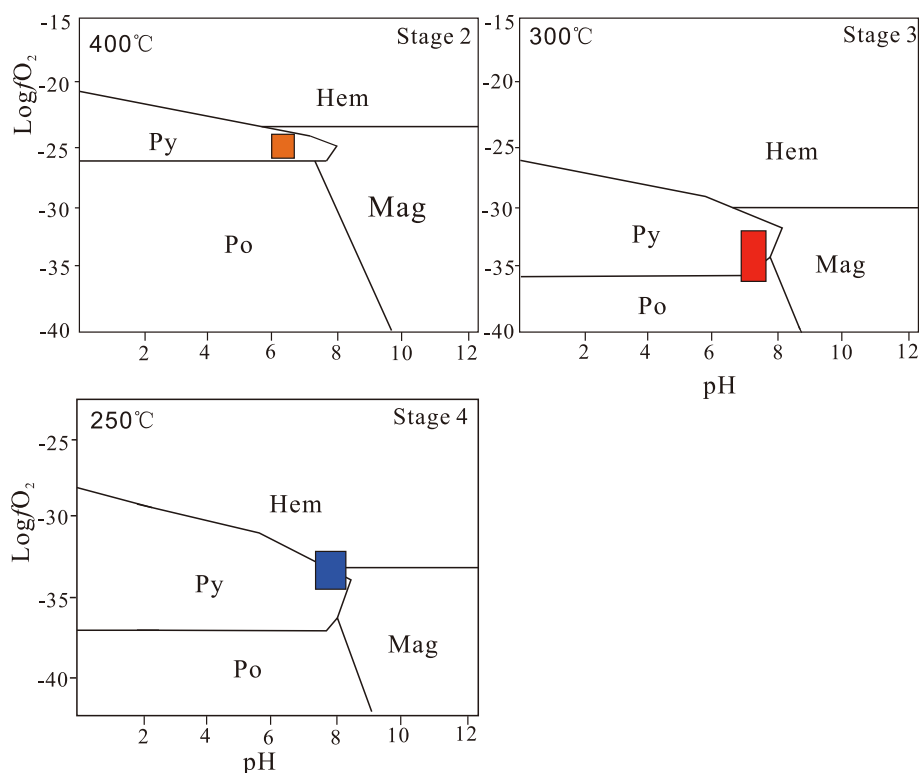
Fig. 14. LogfO_2-pH diagrams showing the field of fO_2 from the Qiyugou gold deposit at 400 °C, 300 °C and 250 °C (drawn by the CHOSZ package of R(Dick, 2008)).

Appendix A. Supplementary data

Supplementary data to this article can be found online at https://doi.org/10.1016/j.oregeorev.2021.104085.

References

Acosta-Góngora, P., Gleeson, S.A., Samson, I.M., Ootes, L., Corriveau, L., 2015. Gold refining by bismuth melts in the iron oxide-dominated NICO Au-Co-Bi (±Cu±W) deposit, NWT. Canada. Econ. Geol. 110, 291–314.

Afifi, A.M., Kelly, W.C., Essene, E.J., 1988a. Phase relations among tellurides, sulfides, and oxides; Pt. II, applications to telluride-bearing ore deposits. Econ. Geol. 83, 395–404.

Afifi, A.M., Kelly, W.C., Essene, E.J., 1988b. Phase relations among tellurides, sulfides, and oxides; I, thermochemical data and calculated equilibria. Econ. Geol. 83, 377–394.

Bi, S.J., Li, J.W., Zhou, M.F., Li, Z.K., 2011. Gold distribution in As-deficient pyrite and telluride mineralogy of the Yangzhaiyu gold deposit, Xiaoqinling district, southern North China craton. Miner. Deposita 46, 925–941.

Brugger, J., Liu, W., Etschmann, B., Mei, Y., Sherman, D.M., Testemale, D., 2016. A review of the coordination chemistry of hydrothermal systems, or do coordination changes make ore deposits? Chem. Geol. 447, 219–253.

Buzatu, A., Damian, G., Dill, H.G., Buzgar, N., Apopei, A.I., 2015. Mineralogy and geochemistry of sulfosalts from Baia Sprie ore deposit (Romania) -New bismuth minerals occurrence. Ore Geol. Rev. 65, 132–147.

Cepedal, A., Fuertes-Fuente, M., Martín-Izard, A., González-Nistal, S., Rodríguez-Pevida, L., 2006. Tellurides, selenides and Bi-mineral assemblages from the Río Narcea Gold Belt, Asturias, Spain: genetic implications in Cu-Au and Au skarns. Mineral. Petrol. 87, 277–304.

Chapman, R.J., Allan, M.M., Mortensen, J.K., Wrighton, T.M., Grimshaw, M.R., 2017. A new indicator mineral methodology based on a generic Bi-Pb-Te-S mineral inclusion signature in detrital gold from porphyry and low/intermediate sulfidation epithermal environments in Yukon Territory, Canada. Miner. Deposita 10, 1007.

Chen, Y.J., Pirajno, F., Li, N., Guo, D.S., Lai, Y., 2009. Isotope systematics and fluid inclusion studies of the Qiyugou breccia pipe-hosted gold deposit, Qinling Orogen, Henan province, China: implications for ore genesis. Ore Geol. Rev. 35, 245–261.

Ciobanu, C.L., Pring, A., Cook, N.J., 2004. Micron- to nano-scale intergrowths among members of the cuprobismutite series and padĕraite: HRTEM and microanalytical evidence. Mineral. Mag. 68, 279–300.

Ciobanu, C.L., Birch, W.D., Cook, N.J., Pring, A., Grundler, P.V., 2010. Petrogenetic significance of Au-Bi-Te-S associations: The example of Maldon, Central Victorian gold province, Australia. Lithos 116, 1–17.

Cockerton, A.B.D., Tomkins, A.G., 2012. Insights into the liquid bismuth collector model through analysis of the Bi-Au stormont skarn prospect, Northwest Tasmania. Econ. Geol. 107, 667–682.

Cook, N.J., Ciobanu, C.L., 2004. Bismuth tellurides and sulphosalts from the Larga hydrothermal system, metaliferi Mts., Romania: paragenesis and genetic significance. Mineral. Mag. 68, 301–321.

Cook, N.J., Ciobanu, C.L., Mao, J., 2009a. Textural control on gold distribution in As-free pyrite from the Dongping, Huangtuliang and Hougou gold deposits, North China Craton (Hebei Province, China). Chem. Geol. 264, 101–121.

Cook, N.J., Ciobanu, C.L., Spry, P.G., Voudouris, P., 2009b. Understanding gold-(silver)-telluride-(selenide) mineral deposits. Episodes 32, 249–263.

Deng, J., Wang, Q., Li, G., Santosh, M., 2014. Cenozoic tectono-magmatic and metallogenic processes in the Sanjiang region, southwestern China. Earth Sci. Rev. 138, 268–299.

Dick, J.M., 2008. Calculation of the relative metastabilities of proteins using the CHNOSZ software package. Geochem. Trans. 9, 10.

Douglas, N., Mavrogenes, J., Hack, A., England, R., 2000. The liquid bismuth collector model: An alternative gold deposition mechanism [abs.]. In: Silbeck, G., Hubble, T.C.T. (Eds.), Understanding planet Earth; searching for a sustainable future; on the starting blocks of the third millennium: 15th Australian Geological Convention Abstracts. Geological Society of Australia, Sydney, p. 135.

Fan, H.R., Hu, F.F., Wilde, S.A., Yang, K.F., Jin, C.W., 2011. The Qiyugou gold-bearing breccia pipes, Xiong'ershan region, central China: fluid-inclusion and stable-isotope evidence for an origin from magmatic fluids. Int. Geol. Rev. 53, 25–45.

Guo, D.S., Chen, Y.J., Qi, J.P., 2007. Isotope geochemistry and ore genesis of the Qiyugou gold deposit, Henan: a synthesis. Geol. Rev. 53, 217–228 (in Chinese with English abstract).

Li, N., Carranza, E.J.M., Ni, Z., Guo, D., 2012. The CO2-rich magmatic-hydrothermal fluid of the Qiyugou breccia pipe, Henan Province, China: implication for breccia genesis and gold mineralization. Geochem. Explorat. Environ. Anal. 12, 147–160.

Liu, J.L., Zhao, S.J., Cook, N.J., Bai, X.D., Zhang, Z.C., Zhao, Z.D., Zhao, H.B., Lu, J., 2013. Bonanza-grade accumulations of gold tellurides in the Early Cretaceous Sandaowanzi deposit, northeast China. Ore Geol. Rev. 54, 110–126.

Liu, Y.S., Hu, Z.C., Gao, S., Detlef, G., Xu, J., Gao, C.G., Chen, H.L., 2008. In-situ analysis of major and trace elements of anhydrous minerals by LA-ICP-MS without applying an internal standard. Chem. Geol. 257, 34–43.

Lu, X.X., Yu, X.D., Yu, Z.P., Wang, Y.T., Xue, L.W., Ye, A.W., Suo, T.Y., Jin, J.P., 2004. Minerogenesis of gold and its coupling with tectonics in Xiaoqinling-Xiong'ershan region. Gold Geol. 10 (1), 1–5 (in Chinese with English abstract).

Mao, J.W., Goldfarb, R.J., Zhang, Z., Xu, W., Qiu, Y., Deng, J., 2002. Gold deposits in the Xiaoqinling-Xiong'ershan region, Qinling mountains, central China. Miner. Deposita 37, 306–325.

Mao, J.W., Xie, G.Q., Bierlein, F., Qü, W.J., Du, A.D., Ye, H.S., Pirajno, F., Li, H.M., Guo, B.J., Li, Y.F., Yang, Z.Q., 2008. Tectonic implications from Re-Os dating of Mesozoic molybdenum deposits in the East Qinling-Dabie orogenic belt. Geochim. Cosmochim. Acta 72, 4607–4626.

Mao, J.W., Xie, G., Pirajno, F., Ye, H., Wang, Y., Li, Y., Xiang, J., Zhao, H., 2010. Late Jurassic-Early Cretaceous granitoid magmatism in Eastern Qinling, central-eastern China: SHRIMP zircon U-Pb ages and tectonic implications. Aust. J. Earth Sci. 57, 51–78.

Makovicky, E., Karup-Møller, S., 1977. Chemistry and crystallography of the lillianite homologous series. Part II: definition of new minerals: eskimoite, vikingite, ourayite and treasurite. Redefinition of schirmerite and new data on the lillianite-gustavite solidisolution series. Neues Jb. Mineral. Abh. 131, 187–207.

Meng, L., Gao, X.Y., Wu, Q., Zhao, T.P., 2020. Mineralization of the Luanling gold deposit in the southern margin of the North China Craton: Insights from mineralogy and mineral chemistry of sulfides, tellurides and oxides. Geol. J. 55, 5831–5849.

Oberthür, T., Weiser, T.W., 2008. Gold-bismuth-telluride-sulphide assemblages at the Viceroy Mine, Harare-Bindura-Shamva greenstone belt, Zimbabwe. Mineral. Mag. 72, 953–970.

Okamoto, H., Massalski, T.B., 1983. The Au-Bi (gold-bismuth) system. Bull. Alloy Phase Diagr. 4, 401–407.

Qi, N., Wang, P., Yu, J., Chen, Y.J., 2019. Geochronology and origin of the Qi189 porphyry gold deposit in Qiyugou Orefield, Qinling Orogen, China. Ore Geol. Rev. 114.

Reich, M., Kesler, S.E., Utsunomiya, S., Palenik, C.S., Chryssoulis, S., Ewing, R.C., 2005. Solubility of gold in arsenian pyrite. Geochim. Cosmochim. Acta 69, 2781–2796.

Shao, K.Z., 1992. Characteristics of Qiyugou gold deposits and their prospecting perspective geological setting. J. Hebei Coll. Geol. 15, 105–195 (in Chinese with English abstract).

Simon, G., Kesler, S.E., Essene, E.J., 1997. Phase relations among selenides, sulfides, tellurides, and oxides II. Applications to selenide-bearing ore deposit. Econ. Geol. 92, 468–484.

Tooth, B., Brugger, J., Ciobanu, C., Liu, W., 2008. Modeling of gold scavenging by bismuth melts coexisting with hydrothermal fluids. Geology 36, 815–818.

Tooth, B., Ciobanu, C.L., Green, L., Neill, O., Brugger, B.J., 2011. Bi-melt formation and gold scavenging from hydrothermal fluids: an experimental study. Geochim. Cosmochim. Acta 75, 5423–5443.

Törmänen, T.O., Koski, R.A., 2005. Gold enrichment and the Bi-Au association in pyrrhotite-rich massive sulfide deposits, Escanaba Trough, Southern Gorda Ridge. Econ. Geol. 100, 1135–1150.

Wang, F.Y., Ge, C., Ning, S., Nie, L., Zhong, G., White, N., 2017. A new approach to LA-ICP-MS mapping and application in geology. Acta Petrol. Sin. 33, 3422–3436 (in Chinese with English abstract).

Wang, P., Mao, J.W., Ye, H.S., Jian, W., Chen, X.D., Tian, Y.F., He, S., Yan, J.M., Wu, S.K., Wan, S.K., 2020. The Qiyugou Au orefield — An intrusion-related gold system in the Eastern Qinling ore belt, China: Constraints from SIMS zircon U-Pb, molybdenite ReOs, sericite 40Ar-39Ar geochronology, in-situ S-Pb isotopes, and mineralogy. Ore Geol. Rev. 124, 1–23.

Wang, Y.T., Mao, J.W., Lu, X.X., 2001. ^{40}Ar-^{39}Ar dating and geochronological constraints on the ore-forming epoch of the Qiyugou gold deposit in Songxian County, Henan Province. Geol. Rev. 47, 551–555 (in Chinese with English abstract).

Xu, W.G., Fan, H.R., Hu, F.F., Santosh, M., Yang, K.F., Lan, T.G., Wen, B.J., 2014. Gold mineralization in the Guilaizhuang deposit, southwestern Shandong Province, China: insights from phase relations among sulfides, tellurides, selenides and oxides. Ore Geol. Rev. 56, 276–291.

Xu, X.S., Griffin, W.L., Ma, X., O'Reilly, S.Y., He, Z.Y., Zhang, C.L., 2009. The Taihua group on the southern margin of the North China craton: further insights from U-Pb ages and Hf isotope compositions of zircons. Mineral. Petrol. 97, 43–59.

Xue, F., Kroner, A., Reischmann, T., Lerch, F., 1996. Paleozoic pre- and post-collision calcalkaline magmatism in the Qinling orogenic belt, central China, as documented by zircon ages on granitoid rocks. J. Geol. Soc. London 153, 406–417.

Yao, J.M., Zhao, T.P., Li, J., Sun, Y.L., Yuan, Z.L., Chen, W., Han, J., 2009. Molybdenite Re-Os age and zircon U-Pb age and Hf isotope geochemistry of the Qiyugou gold system, Henan province. Acta Petrol. Sin. 252, 374–384 (in Chinese with English Abstract).

Zhang, X.M., Spay, P.G., 1994. Calculated stability of aqueous Te species, Calaverite, and Hessitc at elevated temperatures. Econ. Geol. 89, 1152–1166.

Zhao, G.C., Sun, M., Wilde, S.A., Li, S.Z., 2004. A Paleo-Mesoproterozoic supercontinent: assembly, growth and breakup. Earth-Sci. Rev. 67, 91–123.

Zhao, G.C., He, Y., Sun, M., 2009. The Xiong'er volcanic belt at the southern margin of the North China Craton: petrographic and geochemical evidence for its outboard position in the Paleo-Mesoproterozoic Columbia Supercontinent. Gondwana Res. 16, 170–181.

Zhao, T.P., 2000. The characteristics and genesis of the high-K volcanic rocks within the Proterozoic Xiong'er Group at the southern margin of the North China Block. Ph.D. thesis, Institute of Geology and Geophysics, Chinese Academy of Sciences, China, Beijing, pp.1-102 (in Chinese with English abstract).

Zhao, T.P., Zhou, M.F., Zhai, M., Xia, B., 2002, Paleoproterozoic rift-related volcanism of the Xiong'er Group, North China Craton: implications for the breakup of Columbia: Int. Geol. Rev., 44, 336-351.

Zhou, H.Y., Sun, X.M., Fu, Y., Lin, H., Jiang, L.Y., 2016. Mineralogy and mineral chemistry of Bi-minerals: Constraints on ore genesis of the Beiya giant porphyry-skarn gold deposit, southwestern China. Ore Geol. Rev. 79, 408–424.

Zhou, H.Y., Sun, X.M., Cook, N.J., Lin, H., Fu, Y., Zhong, R.C., Brugger, J., 2017. Nano-to micron-scale particulate gold hosted by magnetite: A product of gold scavenging by bismuth melts. Econ. Geol. 112, 993–1010.

Zhou, H., Sun, X., Wu, Z., Yang, T., Li, D., Ren, Y., Liu, Q., Zhu, K., Yu, H., 2018. Mineralogy of Bi-sulfosalts and tellurides from the Yaoan gold deposit, southwest China: Metallogenic implications. Ore Geol. Rev. 98, 126–140.